Singular Higher Order Divergence-Conforming Bases of Additive Kind and Moments Method Applications to 3D Sharp-Wedge Structures

Original

Singular Higher Order Divergence-Conforming Bases of Additive Kind and Moments Method Applications to 3D Sharp-Wedge Structures / Graglia, Roberto; Lombardi, Guido. - In: IEEE TRANSACTIONS ON ANTENNAS AND PROPAGATION. - ISSN 0018-926X. - STAMPA. - 56:12(2008), pp. 3768-3788. [10.1109/TAP.2008.2007390]

Publisher:
IEEE

Published
DOI:10.1109/TAP.2008.2007390

Singular Higher Order Divergence-Conforming Bases of Additive Kind and Moments Method Applications to 3D Sharp-Wedge Structures

Roberto D. Graglia, *Fellow, IEEE*, and Guido Lombardi, *Member, IEEE*

***Abstract*—We present new subsectional, singular divergence-conforming vector bases that incorporate the edge conditions for conducting wedges. The bases are of additive kind because obtained by incrementing the regular polynomial vector bases with other subsectional basis sets that model the singular behavior of the unknown vector field in the wedge neighborhood. Singular bases of this kind, complete to arbitrarily high order, are described in a unified and consistent manner for curved quadrilateral and triangular elements. The higher order basis functions are obtained as the product of lowest order functions and Silvester-Lagrange interpolatory polynomials with specially arranged arrays of interpolation points. The completeness properties are discussed and these bases are proved to be fully compatible with the standard, high-order regular vector bases used in adjacent elements. Our singular bases guarantee normal continuity along the edges of the elements allowing for the discontinuity of tangential components, adequate modelling of the divergence, and removal of spurious solutions. These singular high-order bases provide more accurate and efficient numerical solutions of surface integral problems. Several test-case problems are considered in the paper, thereby obtaining highly accurate numerical results for the current and charge density induced on 3D sharp-wedge structures. The results are compared with other solutions when available and confirm the faster convergence of these bases on wedge problems.**

***Index Terms*—Basis functions, boundary integral equations, curvilinear geometry, electromagnetic analysis, electromagnetic diffraction, electromagnetic scattering, Galerkin method, high-order modelling, method of moments (MoM), numerical analysis, singular vector functions incorporating edge conditions, wedges.**

I. INTRODUCTION

THE method of moments (MoM) is one of the most widely used numerical techniques for solving electromagnetic scattering and radiation problems, and MoM practitioners have been using subsectional vector basis functions defined on planar triangular or quadrilateral patches for more than two decades (see, for example, [1]–[3]). Higher order vector bases on curved patches have been introduced more recently (see [4] and references therein) to reduce the order of the MoM system matrix necessary to get numerical results of a given desired accuracy, as well as to avoid the discretization errors that occur when surfaces with curvature are modelled.

The most useful vector bases for MoM applications are the divergence-conforming ones [3], [4]; these bases guarantee the continuity of the normal component of the vector unknown across adjacent patches (or elements) and are appropriate for the discretization of the electric field integral equation (EFIE) operator. Unfortunately, a deficiency of the commonly used vector bases, including high-order ones, is their inability to accurately model the charge and current densities close to a sharp edge [5, Ch. 10]. It is well known that the charge and current densities near an edge could exhibit a singularity [6], [7]; by including this singularity in the basis functions one can avoid erroneous results near the edge and improve convergence.

The interest in incorporating edge conditions in MoM solutions dates back to the mid seventies of the last century [8], with more recent contributions available in [9]–[12]. In particular, singular higher order complete vector bases of the curl- and divergence-conforming kind have been presented in [12], with several numerical results that confirm the faster convergence of the singular curl-conforming bases on wedge problems modelled by the vector Helmholtz equation. One of the purposes of this paper is to prove that the same holds when singular divergence-conforming bases are used for the MoM solution of wedge problems modelled by integral equations, where incorporation of the edge conditions in the MoM basis functions improves the *numerical* convergence and permits one to avoid erroneous results near the edge. This paper, however, is not intended to provide and does not provide *analytical* results for the rate of convergence of the MoM-solution of integral equations; rather, it shows with several numerical experiments that use of our singular functions provide a substantial reduction of the errors in the near-field region for problems where the induced current density is singular. In fact, to analytically establish the rate of convergence of the MoM-solutions in the singular cases where the induced current density is not square integrable one should work with (negative) fractional-order Sobolev spaces [13]; this analytical study would be even more involved for the three-dimensional cases here considered to fully take into account the use of singular subsectional vector bases of additive kind. As a matter of fact, in general, this kind of analytical study

---

Manuscript received March 19, 2008; revised September 08, 2008. Current version published December 30, 2008. This work was supported by NATO in the framework of the Science for Peace Programme under Grant CBP.MD.SFPP 982376 - *Electromagnetic Signature of Edge-Structures for Unexploded Ordnance Detection*. Patent protection of this work has been filed in Italy with patent application n. TO2003A000675 (publication n. WO2005024674), and extension of patent coverage in other countries is being considered.

R. D. Graglia is with the Dipartimento di Elettronica, Politecnico di Torino, 10129 Torino, Italy and also with ISMB-Istituto Superiore Mario Boella, 10138 Torino, Italy (e-mail: roberto.graglia@polito.it).

G. Lombardi is with the Dipartimento di Elettronica, Politecnico di Torino, 10129 Torino, Italy (e-mail: guido.lombardi@polito.it).

Digital Object Identifier 10.1109/TAP.2008.2007390

can eventually provide only estimates for the current errors (see, for example, [13]) whereas, for example, the results reported in Section V-C for the rate of convergence of our numerical solutions to the exact singular currents are not estimates, but were obtained numerically by comparing our numerical solutions with other exact results available in the literature.

As stated in [12], our singular divergence-conforming bases are intended to deal with impenetrable (conducting) wedges; these bases are directly defined in the parent domain of the elements, incorporate the edge conditions, and are able to approximate the charge and current distributions in the neighborhood of the edge of a wedge for any order of the singularity coefficient ν, that is supposed given and known *a priori*. As noticed in [12], our singular bases contain as a subset the regular bases already discussed in [4], as well as another *Meixner* subset that contains singular terms; this second subset is named after Meixner because it models singular as well as other nonsingular irrational algebraic terms of the Meixner series (see [12, Eq. (1)], [6], [7]). One of the most important features of our singular bases is their additive kind, which consists in the possibility to increment a given singular base with other Meixner subsets, each one associated with a different singularity coefficient. In the simpler case where only one Meixner subset is used, the order of the singular bases is given by a couple $[p, s]$ of integer indexes, where p is the order of the regular part of the base, which completely models regular vector fields and their divergence up to the polynomial order p, while s is the order of the singular part of the basis set [12]. Similarly, the order of bases made of two or more Meixner subsets will be given by a set of integers $[p, s_1, s_2, \ldots, s_m]$, m being the number of the Meixner subsets considered. By use of this notation, the lowest order of the singular bases containing only one Meixner subset is [0, 0] (see [12]).

The present paper modifies some of the singular lowest order divergence-conforming vector basis functions reported in [12, Table III] because those functions model the divergence of the unknown field in a way that is not completely satisfactory under the physical point of view. Furthermore, it turns out that the singular functions of the [0, 0]th order triangular base given in [12, Table III] are constrained by some dependency relationships that need to be considered when multiplying this base times complete higher order polynomials, so to form bases of higher $[p, s]$th order, with $s \geq 1$. Because of their complex expression, those dependencies can hardly be revealed without experimenting on the higher order bases and were overlooked by [12]. The lowest order bases presented in this paper overcome the previous two drawbacks and permit one to straightforwardly build singular higher order complete vector bases of the divergence-conforming kind.

In this paper, in Section II, we briefly revise the Meixner approximation for the current and charge density in the neighborhood of a sharp wedge, to reformulate this approximation in terms of edge- and height-vectors of the elements attached to the edge of the wedge. Our new singular lowest order divergence-conforming bases fulfil the four properties already discussed in [12, Sec. II]; these bases are then presented in Table I of Section III, where we also prove their completeness and discuss their modelling capabilities. In Section IV, singular higher order bases are obtained by forming the product of the lowest order ones with complete Silvester interpolation polynomial factors. Several numerical results are then presented in Section V and, perhaps, before diving for the many mathematical details reported in Sections II–IV, the reader could first go over Table I and Section V to immediately appreciate the advantages provided by the use of these bases. A strong mathematical effort was devoted to derive the Table I bases, thereby trying several *alternative* definition *methods*; one of these alternative methods based on the use of special potentials to define singular divergence-less basis functions is briefly discussed in the Appendix at the end of this paper.

II. SINGULAR ELEMENT REPRESENTATION AND MEIXNER-LIKE APPROXIMATION ON EDGE SINGULARITY ELEMENTS

In the following we assume the reader to be comfortable with the definitions and element representation given in [4], [12], and adopt the same notation used in [12] to present and discuss our new singular divergence-conforming bases. In the neighborhood of the edge profile, the wedge faces are meshed by using edge singularity quadrilaterals and/or two types of singularity triangles: the edge (e) and the vertex (v) singularity triangle, with local edge numbering schemes shown in Fig. 1. The vertex singularity triangles have only one vertex attached to the edge-profile; the presence of these elements is unavoidable whenever a wedge structure is meshed by triangular elements only. With respect to the mesh used in the neighborhood of the wedge region, the vertex singularity triangles are *element fillers* with modelling capability of lower quality (see Section III-D). As already stated in [12], there is no interest in considering vertex singularity quadrilaterals since the only element-filler required to mesh in the neighborhood of the edge profile is the vertex singularity triangle.

The local edge-numbering scheme sketched in Fig. 1 associates the $i \pm 1$ labels to the element edges departing from the edge profile; the behavior of the vector basis functions along these edges, and in the neighborhood of the edge of the wedge, can be given in terms of a dummy variable χ which varies linearly from zero to unity along the $(i \pm 1)$ edges, with $\chi = 0$ on the edge profile and $\chi = 1$ on the vertex opposite to the edge profile [12]. With reference to Fig. 1, one has

$$\chi = \begin{cases} 1 - \xi_i & \text{for vertex singularity triangles} \\ \xi_i & \text{for edge singularity elements} \end{cases} \tag{1}$$

where ξ_i is the normalized element coordinate (parent coordinate) that vanishes on the ith edge of the element and that is equal to unity on the edge or vertex opposite to this ith edge. For edge singularity elements and small χ, the coordinate lines $\chi = const.$ are parallel to the edge-profile because the ith edge $(\xi_i = 0)$ of these elements is lying on the edge-profile [Fig. 1 and (1)]. On the elements of Fig. 1, any vector quantity can be expressed in terms of the mutually orthogonal edge-vector $\boldsymbol{\ell_i}$ and height unit-vector $\hat{\boldsymbol{h}}_i$ defined in [4], with $\hat{\boldsymbol{h}}_i$ parallel to $\boldsymbol{\nabla}\chi$. On each *edge singularity element* χ is equal to ξ_i, and the unit vector normal and tangent to the edge-profile are $\hat{\boldsymbol{h}}_i(\chi = 0)$ and $\boldsymbol{\ell_i}(\chi = 0)$, respectively.

TABLE I
LOWEST ORDER DIVERGENCE-CONFORMING BASES

	Basis Functions	Surface Divergences$^{\heartsuit}$	Dependency Relations
Quadrilateral Base The subscripts are counted modulo 4, for $i = 1, 2, 3$ or 4	Regular Functions [4] $\boldsymbol{\Lambda}_\beta(\boldsymbol{r}) = \frac{\xi_{\beta+2}\,\boldsymbol{\ell}_{\beta-1}}{\mathcal{J}}$ for $\beta = i, i+2, i \pm 1$	$\frac{1}{\mathcal{J}}$	$\xi_{i+1}\,\boldsymbol{\Lambda}_{i+1}(\boldsymbol{r}) + \xi_{i-1}\,\boldsymbol{\Lambda}_{i-1}(\boldsymbol{r}) = 0$ $\xi_i\,\boldsymbol{\Lambda}_i(\boldsymbol{r}) + \xi_{i+2}\,\boldsymbol{\Lambda}_{i+2}(\boldsymbol{r}) = 0$
	Edge Singular Functions$^{\diamondsuit}$ ${}^e\boldsymbol{\Lambda}_{i\pm1}(\boldsymbol{r}) = \left(\nu\xi_i^{\nu-1} - 1\right)\boldsymbol{\Lambda}_{i\pm1}(\boldsymbol{r})$ ${}^e\mathbf{V}_{i+2}(\boldsymbol{r}) = \left(\xi_i^{\nu-1} - 1\right)\boldsymbol{\Lambda}_{i+2}(\boldsymbol{r})$	$\frac{\nu\xi_i^{\nu-1} - 1}{\mathcal{J}}$	$\xi_{i+1}\,{}^e\boldsymbol{\Lambda}_{i+1}(\boldsymbol{r}) + \xi_{i-1}\,{}^e\boldsymbol{\Lambda}_{i-1}(\boldsymbol{r}) = 0$
Triangular Base The subscripts are counted modulo 3, for $i = 1, 2$ or 3	Regular Functions [4] $\boldsymbol{\Lambda}_\beta(\boldsymbol{r}) = \frac{1}{\mathcal{J}}\left(\xi_{\beta+1}\boldsymbol{\ell}_{\beta-1} - \xi_{\beta-1}\boldsymbol{\ell}_{\beta+1}\right)$ for $\beta = i, i \pm 1$	$\frac{2}{\mathcal{J}}$	$\xi_{i+1}\,\boldsymbol{\Lambda}_{i+1}(\boldsymbol{r}) + \xi_{i-1}\,\boldsymbol{\Lambda}_{i-1}(\boldsymbol{r})$ $+\,\xi_i\,\boldsymbol{\Lambda}_i(\boldsymbol{r}) = 0$
	Vertex Singular Functions$^{\clubsuit}$ ${}^v\boldsymbol{\Lambda}_{i\pm1}(\boldsymbol{r}) = \chi_a\boldsymbol{\Lambda}_{i\pm1}(\boldsymbol{r}) \mp \chi_b\,\frac{\xi_{i\mp1}\boldsymbol{\ell}_i}{\mathcal{J}}$ ${}^v\mathbf{V}_i(\boldsymbol{r}) = \chi_a\,\boldsymbol{\Lambda}_i(\boldsymbol{r})$ with $\chi_a = (1-\xi_i)^{\nu-1} - 1$ $\chi_b = (1-\nu)\,(1-\xi_i)^{\nu-2}$	$\frac{(1+\nu)\,(1-\xi_i)^{\nu-1} - 2}{\mathcal{J}}$	$\xi_{i+1}\,{}^v\boldsymbol{\Lambda}_{i+1}(\boldsymbol{r}) + \xi_{i-1}\,{}^v\boldsymbol{\Lambda}_{i-1}(\boldsymbol{r})$ $+\,\xi_i\,{}^v\mathbf{V}_i(\boldsymbol{r}) = 0$
	Edge Singular Functions$^{\diamondsuit,\spadesuit}$ ${}^e\boldsymbol{\Lambda}_{i\pm1}(\boldsymbol{r}) = \left(\nu\xi_i^{\nu-1} - 1\right)\boldsymbol{\Lambda}_{i\pm1}(\boldsymbol{r})$	$\frac{\nu\,(1+\nu)\,\xi_i^{\nu-1} - 2}{\mathcal{J}}$	$\xi_{i+1}\,{}^e\boldsymbol{\Lambda}_{i+1}(\boldsymbol{r}) + \xi_{i-1}\,{}^e\boldsymbol{\Lambda}_{i-1}(\boldsymbol{r})$ $+\,\xi_i\,{}^g\boldsymbol{\Lambda}_i(\boldsymbol{r}) = 0$

♡ All the basis functions appearing in each row have identical surface divergence. In particular, for the singular functions, (1) yields $\boldsymbol{\nabla}\cdot{}^e\boldsymbol{\Lambda}_{i\pm1}(\boldsymbol{r}) = \boldsymbol{\nabla}\cdot{}^e\mathbf{V}_{i+2}(\boldsymbol{r}) = \left[\nu\chi^{\nu-1} - 1\right]/\mathcal{J}$ for the quadrilateral base; $\boldsymbol{\nabla}\cdot{}^v\boldsymbol{\Lambda}_{i\pm1}(\boldsymbol{r}) = \boldsymbol{\nabla}\cdot{}^v\mathbf{V}_i(\boldsymbol{r}) = \left[(1+\nu)\,\chi^{\nu-1} - 2\right]/\mathcal{J}$ for the vertex singularity triangle, and $\boldsymbol{\nabla}\cdot{}^e\boldsymbol{\Lambda}_{i\pm1}(\boldsymbol{r}) = \left[\nu\,(1+\nu)\,\chi^{\nu-1} - 2\right]/\mathcal{J}$ for the edge singularity triangle.

◇ The edge singular functions are singular on the i-th edge (where $\xi_i = 0$), and vanish for $\nu = 1$.

♣ The vertex singular functions are singular at the vertex $\xi_i = 1$, and vanish for $\nu = 1$.

♠ The *ghost* function ${}^g\boldsymbol{\Lambda}_i(\boldsymbol{r}) = \left(\nu\xi_i^{\nu-1} - 1\right)\boldsymbol{\Lambda}_i(\boldsymbol{r})$ appearing in the dependency relation at right does not belong to the edge singular triangular basis set because its divergence contains a non-physical $\xi_i^{\nu-2}$ term. Although the divergence of the higher-order edgeless function $\xi_i\,{}^g\boldsymbol{\Lambda}_i(\boldsymbol{r})$ is physical (see (17)), the algorithm to construct independent higher-order edge-singular triangular bases has to discard all the functions obtained by multiplying the ghost function times a polynomial of the parent variables because of the reported dependency relation, or because the divergence of these functions contains non-physical hyper-singular terms.

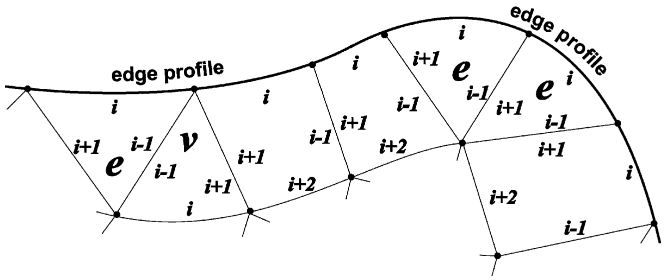

Fig. 1. Edge singularity quadrilaterals and edge ($\boldsymbol{e}$) and vertex ($\boldsymbol{v}$) singularity triangles with local edge numbering scheme. The vertex singularity triangles have only one vertex attached to the edge-profile, whereas the ith edge of each singularity element lies on the edge-profile. Two edge-singularity elements can have a common edge, but the singular basis functions cannot model a corner singularity.

A. Meixner Approximation and Singularity Coefficients for a Sharp Rectilinear Wedge

For a sharp *rectilinear* wedge, in terms of the χ variable and for $\chi \simeq 0$, the approximate behavior of the surface current $\boldsymbol{J}$ and of the charge density ρ on each *edge-singularity* element takes the following form (only the leading order terms of the series considered in [6], [7], [14], [15] are reported)

$$\boldsymbol{J} \simeq \chi^{\nu-1} A_M \boldsymbol{\ell}_{i,\chi=0} - \chi^{\nu} B_M \hat{\boldsymbol{h}}_{i,\chi=0} \tag{2}$$

$$\rho \simeq \nu\chi^{\nu-1} C_M \tag{3}$$

where ν (typically not an integer) is a frequency independent singularity coefficient known *a priori*, whereas A_M, B_M and C_M are appropriate coefficients which change element by element and depend on the material and geometrical properties of the wedge, as well as on the geometrical configuration, angular frequency and polarization of the electromagnetic sources [7]. On each element, C_M is related to A_M and B_M by the continuity equation; if A_M is constant, C_M is related only to B_M and the *longitudinal* current component (in the $\boldsymbol{\ell}_{i,\chi=0}$ direction) is divergence-less.

A complication of the wedge problem is due to the fact that the current and charge densities in the wedge neighborhood exhibit, in principle, infinite terms of the form (2), (3), each one relevant to a singularity coefficient of a different ν-value [7], [14]–[16]. For example, Fig. 2 shows the behavior of the lower

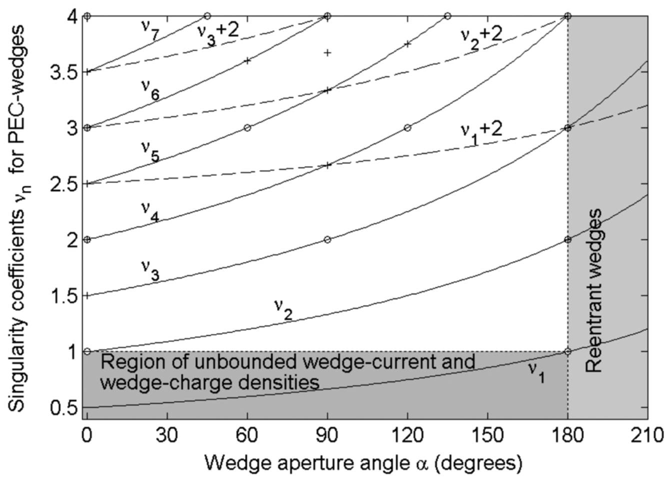

Fig. 2. Singularity coefficients ν_n for a PEC-wedge of aperture angle α [7], in the range $\{0 \leq \alpha \leq 210^\circ, \nu_n \leq 4\}$. The dashed-lines show the coefficients $\overline{\nu} = \nu_n + 2m$ ($m = \{1, \infty\}$ and integer) associate to terms of the form $\chi^{\overline{\nu}}$; these terms arise by expanding in series the Bessel functions of fractional order which appear in the rigorous solution of the infinite straight-wedge problem [15], [16]. Integer values of the singularity coefficients are marked by circles; all the coefficients become integer at $\alpha = 180^\circ$ (flat plate) and at $\alpha = 270^\circ$. The plus marker shows the points $\nu_i + k = \nu_j + \ell$, for $k, \ell \geq 0$ and integer, and $\nu_i \neq \nu_j$. In the figure, these points occur only at $\alpha = 60^\circ, 90^\circ, 120^\circ$, and 180°; only the *plus* point ($\alpha = 90^\circ, \nu_1 + 3 = \nu_4 + 1 = 11/3$) does not belong to any of the reported lines. Furthermore, in the region $\{0 \leq \alpha < 360^\circ, \nu_n \leq 4\}$, the solutions of $\nu_1 + k = \nu_2 + \ell$ occur only at $\alpha = 180^\circ$ and $\alpha = 270^\circ$, where ν_1 and ν_2 are both integer.

singularity coefficients ν_n (for $n \leq 7$) of a perfect electric conducting (PEC)-wedge as functions of the wedge aperture angle α (see [7]). For the sake of completeness, Fig. 2 reports by dashed-lines also the singularity coefficients $\nu_n + 2m$ (with integer $m = \{1, \infty\}$) obtained by expanding in series the Bessel functions of fractional order that appear in the rigorous solution of the infinite straight-wedge problem [15], [16]. It is instructive to note in Fig. 2 that, as the PEC-wedge degenerates to a flat plate ($\alpha = 180^\circ$), all the terms of the form (2), (3) degenerate into higher order polynomial forms (with integer $\nu_n = n$) that can be modelled by regular higher order divergence-conforming bases.

A further complication occurs for source and scatterer configurations with particular symmetry [7], [16], [17], where some of the field singularities are not excited and where the dominant singular term is different from the leading one, that is when the A_M, B_M and C_M coefficients relative to the lowest ν-value vanish. The bases presented in this paper permit one to deal with these problems because of their additive kind. In fact, although this paper presents bases able to deal with only one singular ν-term of the form (2), (3), one can easily *enlarge* the bases to include other Meixner's subsets able to model different singular terms $(\nu_1, \nu_2, \ldots)$ up to a prescribed order ν_m. For the sake of brevity, this extension is omitted in this paper because of three reasons. First of all, this extension is rather simple, although it requires numerical integration schemes more sophisticated than those required to consider just the dominant singular term. Secondly, MoM practitioners are particularly interested in including in their numerical models the strongest singularity, that is the field behavior [(2), (3)] for ν less than unity. Finally, as opposite to what happens for $\nu < 1$, the field behavior relative to a non integer singularity coefficient $\nu_n > 1$ can be approximately modelled with good results by regular vector polynomial basis functions of higher order, that is by using $[p, s]$-bases with $p \geq 1$.

B. The Meixner-Like Approximation for a Sharp Wedge With Curved Edge-Profile

We now consider a wedge with a curved edge-profile meshed by curved singular elements (Fig. 1). In this case, in view of numerical applications of the MoM technique and in order to discuss the results of Section III, it is convenient to generalize [(2), (3)] and postulate the following local behavior in terms of the variable edge ($\boldsymbol{\ell}_i$) and height ($\hat{\boldsymbol{h}}_i$) vectors of each edge-singularity element [18]

$$\boldsymbol{J} \simeq \chi^{\nu-1}\frac{A}{\mathcal{J}}\boldsymbol{\ell}_i - \chi^{\nu}\frac{B}{\ell_i}\hat{\boldsymbol{h}}_i \qquad (4)$$

$$\rho \simeq \nu\chi^{\nu-1}\frac{C}{\mathcal{J}} \qquad (5)$$

where ν is again known a priori (see Fig. 2 for PEC-wedges), $\mathcal{J}$ is the Jacobian of the edge-singularity element, ℓ_i is the magnitude of the edge-vector $\boldsymbol{\ell}_i$, and A, B and C are appropriate variable coefficients, with C related to A and B by the continuity equation. Once again, if A is constant or χ dependent, the longitudinal current component (in the $\boldsymbol{\ell}_i$ direction) is divergence-less because $\boldsymbol{\nabla} \cdot (\boldsymbol{\ell}_i/\mathcal{J}) = 0$ (see [4, Appendix]) and because of the orthogonality of $\boldsymbol{\ell}_i$ and $\boldsymbol{\nabla}\chi$. Notice that (4), (5) agree with (2), (3), in case of rectilinear triangular and rectangular elements, where $\mathcal{J}$, $\boldsymbol{\ell}_i = \boldsymbol{\ell}_i(\chi = 0)$ and $\hat{\boldsymbol{h}}_i = \hat{\boldsymbol{h}}_i(\chi = 0)$ are constant. Equations (2)–(5) are valid only for $\chi \simeq 0$ and neglect higher order terms of the χ variable.

The lowest order Meixner subsets discussed in Section III model (4), (5) in case of constant A, B and C coefficients, whereas the higher order subsets model the case of non constant A, B and C coefficients, and other higher order terms not explicitly reported in (4), (5). Obviously, higher order bases can model (4), (5) in case A, B and C vary along the edge-profile, that is along constant χ coordinate lines.

III. SINGULAR LOWEST ORDER COMPLETE DIVERGENCE-CONFORMING BASES

Table I reports the new singular divergence-conforming bases of the [0, 0]-order for quadrilateral and triangular elements together with their dependency relations, to be discussed in detail in Section IV. These bases contain the regular zeroth-order bases of [4], which are also reported at top of each sub-table forming Table I. For example, the [0, 0]-order base of the vertex singularity triangle is the union of the regular triangular basis set with the three vertex singular functions of Table I. The quadrilateral and triangular edge-singularity element have three and two singular functions, respectively; for these elements, once again, the [0, 0]-order base is formed by the union of the regular set with the corresponding singular-functions set of Table I. To guarantee the additive nature of the bases, all the singular basis functions of Table I vanish at $\nu = 1$, which is the ν value where (2)–(5) are already modelled by regular basis functions.

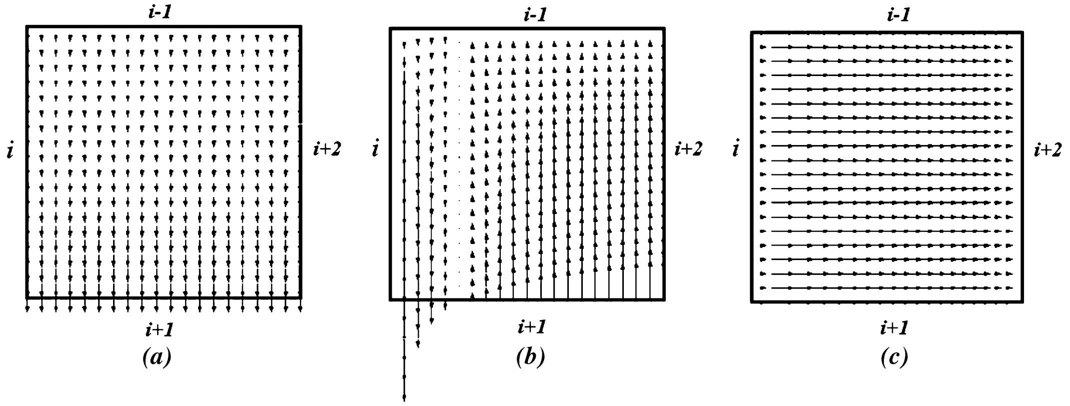

Fig. 3. Quadrilateral basis functions of the lowest order set. (a) The regular function $\mathbf{\Lambda}_{i+1}(\boldsymbol{r})$, (b) edge singular function ${}^{e}\mathbf{\Lambda}_{i+1}(\boldsymbol{r})$, (c) edge singular function ${}^{e}\mathbf{V}_{i+2}(\boldsymbol{r})$. Notice that ${}^{e}\mathbf{V}_{i+2}(\boldsymbol{r})$ is edge-less.

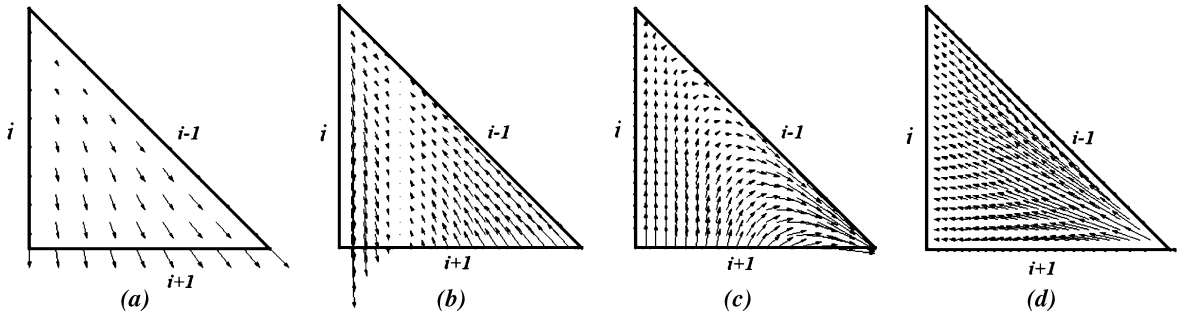

Fig. 4. Triangular basis functions of the lowest order set. (a) The regular function $\mathbf{\Lambda}_{i+1}(\boldsymbol{r})$, (b) edge singular function ${}^{e}\mathbf{\Lambda}_{i+1}(\boldsymbol{r})$, (c) vertex singular function ${}^{v}\mathbf{\Lambda}_{i+1}(\boldsymbol{r})$, (d) the vertex singular function ${}^{v}\mathbf{V}_{i}(\boldsymbol{r})$. Notice that ${}^{v}\mathbf{V}_{i}(\boldsymbol{r})$ is edge-less.

A vector field plot of the quadrilateral and triangular basis functions of Table I is reported in Figs. 3 and 4, respectively.

In the following subsections we illustrate the modelling properties of these bases, particularly of their Meixner subsets with reference to (4), (5).

A. Conformity of the Lowest Order Bases

As shown in [4], the regular functions $\mathbf{\Lambda}_{\beta}(\boldsymbol{r})$ given in Table I have, for rectilinear elements, a constant normal component and a linear tangential (CN/LT) component along each element edge; for curvilinear elements the variation is more complicated because the edge vectors and the Jacobian $\mathcal{J}$ also vary along the edge, but the normal components remain continuous across element boundaries. However, in this subsection we consider in detail only the Meixner subsets of our bases, since conformity of the regular subsets is thoroughly discussed in [4].

The singular functions ${}^{e}\mathbf{V}_{i+2}$ and ${}^{v}\mathbf{V}_{i}$ of the quadrilateral and triangular set, respectively, are element-based because they have a vanishing normal component along each of the element edges. To reflect the edgeless property, the symbol used to represent ${}^{e}\mathbf{V}_{i+2}$ and ${}^{v}\mathbf{V}_{i}$ has been obtained by overturning $\mathbf{\Lambda}$. The subscripts $(i+2)$ and i still appear in these symbols merely because ${}^{e}\mathbf{V}_{i+2}$ is given in terms of the *regular* quadrilateral function $\mathbf{\Lambda}_{i+2}(\boldsymbol{r})$, whereas ${}^{v}\mathbf{V}_{i}$ is given in terms of the *regular* triangular function $\mathbf{\Lambda}_{i}(\boldsymbol{r})$. The remaining singular functions of Table I, as well as all the regular functions, are edge-based and associated only with the edge quoted in their subscript, since the normal component of these functions along the other element edges (not quoted in the subscript) is always equal to zero. Irrespective of whether one considers the quadrilateral or the triangular element, the normal component of the edge-based singular functions along side β, for $\beta = i \pm 1$, always reads as follows:

$$ {}^{e}\mathbf{\Lambda}_{\beta}(\boldsymbol{r}) \cdot \hat{\boldsymbol{h}}_{\beta}\Big|_{\xi_{\beta}=0} = {}^{v}\mathbf{\Lambda}_{\beta}(\boldsymbol{q}r) \cdot \hat{\boldsymbol{h}}_{\beta}\Big|_{\xi_{\beta}=0} = \frac{\nu\chi^{\nu-1}-1}{\ell_{\beta}} \quad (6) $$

where ℓ_{β} is the magnitude of the edge-vector $\boldsymbol{\ell}_{\beta}$ at $\xi_{\beta}=0$ and $\hat{\boldsymbol{h}}_{\beta}(\xi_{\beta}=0)$ is the unit outward normal to the element along the βth boundary edge. Recall that ℓ_{β} and $\hat{\boldsymbol{h}}_{\beta}$ are not constant along the βth boundary edge of a curved element, and that χ is zero along the edge profile shown in Fig. 1, with $\chi = \xi_{i}$ or $\chi = (1-\xi_{i})$ for ${}^{e}\mathbf{\Lambda}_{\beta}(\boldsymbol{r})$ and ${}^{v}\mathbf{\Lambda}_{\beta}(\boldsymbol{r})$, respectively [see (1)].

Our basis functions are conforming to adjacent zeroth-order regular elements attached to the ith edge of the singular element, and to the $(i+2)$th edge of the edge singularity quadrilateral. In fact, in our bases, only the regular function $\mathbf{\Lambda}_{i}(\boldsymbol{r})$ and the regular quadrilateral function $\mathbf{\Lambda}_{i+2}(\boldsymbol{r})$ have a non-vanishing normal component along these edges. As far as the two remaining edges $(i \pm 1)$ are concerned, conformity to adjacent elements is ensured in the usual way [4], [12], since the normal component of our basis functions along their associated edge is either regular (for $\mathbf{\Lambda}_{i\pm1}(\boldsymbol{r})$) or singular (for ${}^{e}\mathbf{\Lambda}_{i\pm1}(\boldsymbol{r})$, ${}^{v}\mathbf{\Lambda}_{i\pm1}(\boldsymbol{r})$), with the singular normal component taking the general form (6). Hence, to ensure normal continuity across element boundaries, one has only to fix the sign of these functions in accordance to an arbitrarily selected reference direction across adjacent elements.

B. Completeness to the Regular Zeroth-Order

The bases of Table I are complete to the regular zeroth-order because they contain the regular zeroth-order base (see [4]). This permits one to deal with all cases where the singularity of the fields is not excited and does not require one to limit the size of the mesh in the neighborhood of the edge of the wedge (i.e., sub-meshing is not required). The regular zeroth-order base can also model the nonsingular divergence-less part of the current component normal to the edge of the wedge, whenever this current is present, as opposite to what happens when using the singular bases of non-additive kind given in [11] (see, in particular, [11, Sec. V: Conclusion]).

C. Completeness to the Singular Lowest Order

Equations (7)–(9), (11), and (12) prove that our Table I bases are able to model the leading terms [(4), (5)] of the Meixner series in case of constant A, B, and C coefficients; for this reason we call these bases complete to the singular lowest order, and the bases of Table I of [0, 0]th order.

Completeness of the Longitudinal Vector Component to the $(\nu-1)$*th Order:* The longitudinal component of the current density in the neighborhood of the wedge, whenever singular, varies as $A\chi^{\nu-1}\ell_i/\mathcal{J}$, where A is an appropriate coefficient [see (4)]. This behavior is properly modelled by the basis functions of the edge singularity elements of Table I. In fact, irrespective of whether one considers the edge singularity triangle or quadrilateral, the singular current component parallel to the edge profile (i.e., parallel to the ith edge) is modelled by the following divergence-less linear combination of the lowest order edge-singularity basis functions:

$$\chi^{\nu-1}\frac{\boldsymbol{\ell}_i}{\mathcal{J}} = \frac{1}{\nu}\left\{\left[\boldsymbol{\Lambda}_{i+1}(\boldsymbol{r}) + {}^{e}\boldsymbol{\Lambda}_{i+1}(\boldsymbol{r})\right] - \left[\boldsymbol{\Lambda}_{i-1}(\boldsymbol{r}) + {}^{e}\boldsymbol{\Lambda}_{i-1}(\boldsymbol{r})\right]\right\}. \tag{7}$$

Completeness of the Normal Vector Component to the ν*th-Order:* In terms of the variable χ, the normal component of the current density at the edge of the wedge vanishes as $-\chi^{\nu}B/\ell_i$ [second term on the right-hand side of (4)]. This behavior is properly modelled by the basis functions of the edge singularity elements of Table I. In fact, for the edge singularity triangle, one contains

$$-\frac{\chi^{\nu}}{\ell_i} = \frac{1}{\nu}\left[\boldsymbol{\Lambda}_{i\pm1}(\boldsymbol{r}) + {}^{e}\boldsymbol{\Lambda}_{i\pm1}(\boldsymbol{r})\right]\cdot\hat{\boldsymbol{h}}_i \tag{8}$$

where the two different and independent vector terms $[\boldsymbol{\Lambda}_{i\pm1}(\boldsymbol{r}) + {}^{e}\boldsymbol{\Lambda}_{i\pm1}(\boldsymbol{r})]/\nu$ on the right-hand side of (8) are exactly those subtracted on the right-hand side of (7). Similarly, for the edge singularity quadrilateral, one has

$$-\frac{\chi^{\nu}}{\ell_i} = \left[\boldsymbol{\Lambda}_{i+2}(\boldsymbol{r}) + {}^{e}\mathbf{V}_{i+2}(\boldsymbol{r})\right]\cdot\hat{\boldsymbol{h}}_i \tag{9}$$

where one can further notice that the quadrilateral functions associated with the $(i\pm1)$th edge do not contribute to the current component normal to the edge profile since, in the quadrilateral case, one has

$$\boldsymbol{\Lambda}_{i\pm1}(\boldsymbol{r})\cdot\hat{\boldsymbol{h}}_i = {}^{e}\boldsymbol{\Lambda}_{i\pm1}(\boldsymbol{r})\cdot\hat{\boldsymbol{h}}_i = 0 \tag{10}$$

This latter result together with (9) explains why, for the edge singularity quadrilateral, one needs to introduce the edgeless function ${}^{e}\mathbf{V}_{i+2}(\mathbf{r})$ to properly model the normal component of the current density; conversely, no edgeless function is needed for the edge singularity triangle because of (8).

Divergence Completeness to the $(\nu-1)$*th-Order:* The charge density in the neighborhood of the wedge, whenever singular, varies as $\nu\chi^{\nu-1}C/\mathcal{J}$ [see (5)], with χ given in (1) and where C is an appropriate coefficient. This behavior is properly modelled by the divergence of the basis functions of the Meixner subsets of Table I, as apparent by considering the following (twelve) linear combinations of the quadrilateral basis functions, for $\beta = i, i\pm1, i+2$

$$\nu\frac{\chi^{\nu-1}}{\mathcal{J}} = \boldsymbol{\nabla}\cdot\begin{cases}{}^{e}\boldsymbol{\Lambda}_{i\pm1}(\boldsymbol{r}) + \boldsymbol{\Lambda}_{\beta}(\boldsymbol{r})\\ {}^{e}\mathbf{V}_{i+2}(\boldsymbol{r}) + \boldsymbol{\Lambda}_{\beta}(\boldsymbol{r})\end{cases} \tag{11}$$

as well as by the following linear combinations of the triangular basis functions, for $\beta = i, i\pm1$

$$\begin{aligned}\nu\frac{\chi^{\nu-1}}{\mathcal{J}} &= \frac{1}{(1+\nu)}\boldsymbol{\nabla}\cdot\left[{}^{e}\boldsymbol{\Lambda}_{i\pm1}(\boldsymbol{r}) + \boldsymbol{\Lambda}_{\beta}(\boldsymbol{r})\right]\\ &= \frac{\nu}{(1+\nu)}\boldsymbol{\nabla}\cdot\begin{cases}{}^{v}\boldsymbol{\Lambda}_{i\pm1}(\boldsymbol{r}) + \boldsymbol{\Lambda}_{\beta}(\boldsymbol{r})\\ {}^{v}\mathbf{V}_{i}(\boldsymbol{r}) + \boldsymbol{\Lambda}_{\beta}(\boldsymbol{r}).\end{cases}\end{aligned} \tag{12}$$

D. The Vertex-Singularity Triangle Special Peculiarities

Wedge-structures are often meshed by using vertex-singularity triangles (VST) as *element-fillers*. These elements have only one vertex attached to the edge of the wedge, which is called the VST singular vertex. The singular vertex of a VST is a point of possible discontinuity for the vector tangent to the edge-profile. As opposite to what happens for edge-singularity elements, this wedge tangent-vector cannot be evaluated by using only the geometrical information relative to the VST, even when this tangent vector is continuous on the VST singular vertex (as in the case of a straight wedge). For a VST, (4) is meaningless because the vectors tangent and normal to the edge-profile are not defined on the VST singular vertex; for example, at the singular vertex, the edge-vector $\boldsymbol{\ell}_i$ of a VST is in general not tangent to the edge-profile because the ith edge of a VST is always opposite to the edge-profile (see Fig. 1).

Thus, the vector base associated with a VST is simply obtained by imposing its conformity to adjacent elements, the *regular* zeroth-order completeness of the base, and its capability to model a singular divergence in the wedge neighborhood. In spite of this limitation, it is interesting to observe that results similar to (7), (8) and (9) are obtained by combining the basis functions of the vertex singularity triangle as follows:

$$\begin{aligned}\chi^{\nu-1}\frac{\boldsymbol{\ell}_i}{\mathcal{J}} = \frac{1}{\nu}\{&\left[\boldsymbol{\Lambda}_{i+1}(\boldsymbol{r}) + {}^{v}\boldsymbol{\Lambda}_{i+1}(\boldsymbol{r})\right]\\ &- \left[\boldsymbol{\Lambda}_{i-1}(\boldsymbol{r}) + {}^{v}\boldsymbol{\Lambda}_{i-1}(\boldsymbol{r})\right]\}\end{aligned} \tag{13}$$

$$-\frac{\chi^{\nu}}{\ell_i} = -\left[\boldsymbol{\Lambda}_{i}(\boldsymbol{r}) + {}^{v}\mathbf{V}_{i}(\boldsymbol{r})\right]\cdot\hat{\boldsymbol{h}}_i. \tag{14}$$

In case of smooth edge-profiles, the above equations merely show that it is convenient to make the ith edge of each VST parallel to the edge-profile, whenever this is possible. If this is done, not only (14) still holds (with $\hat{\boldsymbol{h}}_i$ possibly normal to the edge-profile), but the expansion coefficients of the vertex singular functions ${}^v\mathbf{\Lambda}_{i+1}$ and ${}^v\mathbf{\Lambda}_{i-1}$ could result to be numerically equal but with opposite sign, so to yield to a divergence-less term of the form

$$ {}^v\mathbf{\Lambda}_{i+1}(\boldsymbol{r}) - {}^v\mathbf{\Lambda}_{i-1}(\boldsymbol{r}) = \frac{1-(1-\nu)\chi^{\nu-1}}{\mathcal{J}}\boldsymbol{\ell}_i \qquad (15) $$

Since the equality (but for the sign) of the expansion coefficients of ${}^v\mathbf{\Lambda}_{i+1}$ and ${}^v\mathbf{\Lambda}_{i-1}$ can be numerically obtained only within a limited number of figures, it is of importance to point out that it is not convenient to force this equality from the outset, otherwise one would risk to numerically force current components of the form of (15) also in the geometrical region (which could be relatively wide) covered by the edge-singularity elements attached to the VST, where these singular components could be weak or not present.

The reason why VSTs are prone to yield numerical results not completely satisfactory in the neighborhood of their singular vertex is due to the fact that VSTs do not properly model the current component normal to the edge-profile (whenever it makes sense to define it) because of (6), which is a mandatory equation needed to guarantee the element conformity. In this connection, we further observe that vertex-singularity triangles usually spoil the condition number of the MoM system matrix. For these reasons, in order to guarantee good numerical results, one should avoid using on each wedge-face two (or more) vertex-singularity triangles with a common singular vertex; if this occurs, the mesh should be locally modified to merge into one element the VSTs with a common vertex (though, for example, we have not done this to the mesh used to get the results of Fig. 18). Actually, it would be better not to use VSTs, but rather mesh the structure in the wedge neighborhood by using only edge-singularity triangles and quadrilaterals. Although we warn the reader not to use VSTs whenever possible, all the meshes used to obtain the results of Section V contain several elements of this kind to show that vertex singularity triangles can be used with caution to obtain good results although, possibly, these results could not be completely satisfactory in the vicinity of the singular vertex of each VST.

In spite of the fact that the wedge-modelling properties of the vertex singularity triangle are not as good as those of the edge-singularity elements, the vertex singularity triangle counts three singular basis functions, that is one function more than those of the edge-singularity triangle. This higher number of degrees of freedom is not surprising because, as said, two of the VST functions are needed to guarantee element conformity, while the third is needed to model the singular divergence of the unknown surface field (i.e., the charge density). As a matter of fact, the two edge-based singular functions ${}^v\mathbf{\Lambda}_{i\pm1}(\boldsymbol{r})$ are obtained by superimposing the edge-less function ${}^v\mathbf{V}_i(\boldsymbol{r})$ to the two divergence-less functions $[{}^v\mathbf{\Lambda}_{i\pm1}(\boldsymbol{r}) - {}^v\mathbf{V}_i(\boldsymbol{r})]$, which are just those required to guarantee conformity to adjacent elements.

IV. SINGULAR HIGHER ORDER DIVERGENCE-CONFORMING BASES

Higher order bases are obtained by multiplying the lowest order basis sets times complete higher order polynomials. In the following, we illustrate the procedure to form higher order bases that contain only one Meixner subset, thereby starting from the lowest order bases of [0, 0]th order given in Table I. If one considers m different singularity coefficients $(\nu_1, \nu_2, \ldots, \nu_m)$, the order of the lowest order base where to start from would be specified by the array $[0, 0_1, 0_2, \ldots, 0_m]$, made of $m+1$ zeroes.

The set of the polynomial factors used to build the higher order singular bases could take one of several different forms (see [4]). However, for this construction, we prefer to use the Silvester-Lagrange interpolation polynomial factors already used in [4], [12], and explicitly reported in [12, Table I]. The regular part of the $[p, s]$-order bases is built by using polynomial factors of (integer) order p, whereas the higher order Meixner set is obtained by using complete polynomials of (integer) order s.

As discussed in [4], [12], for values of p, $s \geq 1$ the vector functions obtained in this manner are not linearly independent (that is, they are not unisolvent [19]). In contrast to other forms of the bases, these dependencies are particularly easy to spot for higher order bases obtained by use of interpolatory polynomials. In this case, the dependencies occur only if the polynomial factor interpolates an element *internal point*, and one easily individuates those dependencies just by considering the *dependency relations* reported on the right-hand column of Table I which, for the regular basis subsets, were thoroughly discussed in [4].

A. Dependency Relations

The dependency relations in Table I are all written in terms of the vector functions belonging to the lowest order bases, with the exception of the dependency relation valid for the edge-singular triangular functions ${}^e\mathbf{\Lambda}_{i\pm1}(\boldsymbol{r})$. In fact, this relationship is given in terms of the *ghost* function

$$ {}^g\mathbf{\Lambda}_i(\boldsymbol{r}) = \left(\nu\xi_i^{\nu-1} - 1\right)\mathbf{\Lambda}_i(\boldsymbol{r}) \qquad (16) $$

which does not belong to the lowest order edge-singular triangular set because its divergence contains a non-physical $\xi_i^{\nu-2}$ term (to be more specific, this term is hyper-singular and clearly non-physical for ν less than unity). In spite of the fact that the divergence of the higher order *edgeless* function $\xi_i^g\mathbf{\Lambda}_i(\boldsymbol{r})$ is physical, with

$$ \nabla\cdot[\xi_i^g\mathbf{\Lambda}_i(\boldsymbol{r})] = \frac{\left[\nu^2\xi_i^{\nu-1} - 1 + \nu(2-\nu)\xi_i^{\nu} - \xi_i\right]}{\mathcal{J}} \qquad (17) $$

the algorithm to construct independent higher order bases has to discard *all* the functions obtained by multiplying the ghost function ${}^g\mathbf{\Lambda}_i(\boldsymbol{r})$ times a polynomial of the parent variables (hence, also the function $\xi_i^g\mathbf{\Lambda}_i(\boldsymbol{r})$ must be discarded) because of the dependency relation reported in Table I (case a), or because the divergence of these functions contains non-physical hyper-singular terms (case b). Case (a) occurs whenever the Silvester-Lagrange multiplying polynomial contains a ξ_i factor, whereas case (b) considers all the remaining interpolation polynomials that do not contain the ξ_i factor. These latter Silvester-Lagrange polynomials, which do not vanish at $\xi_i = 0$, are exactly those interpolating points along the ith triangular edge [4].

With reference to the edgeless function $\xi_i^g \mathbf{\Lambda}_i(\boldsymbol{r})$ just discussed, which has to be discarded, we notice that the edge-singular triangular base reported in [12] erroneously contains an edgeless function ${}^e\mathbf{V}_i(\boldsymbol{r})$. Actually, this latter function must also be excluded from the lowest order base because it does not model the divergence in a satisfactory way; in fact, the divergence of ${}^e\mathbf{V}_i(\boldsymbol{r})$ given in [12] is singular at the two vertices $\xi_{i\pm 1} = 1$ of the triangular element. As a matter of fact one does not need to introduce any edgeless function for the edge singularity triangle because, as previously noticed in this paper [see (8)], the vanishing current component normal to the edge of the wedge is already modelled by the functions ${}^e\mathbf{\Lambda}_{i\pm 1}(\boldsymbol{r})$ of Table I; in this connection, notice also that the edge-singular triangular functions ${}^e\mathbf{\Lambda}_{i\pm 1}(\boldsymbol{r})$ given in [12, Table III] already have this modelling capability.

Thus, with respect to the singular triangular functions of [12, Table III], the new singular lowest order functions of Table I exhibit two important features. First of all, the dependency relations of Table I are quite simple, whereas the dependencies of the singular higher order triangular functions of [12] can hardly be revealed without experimenting. Secondly, the divergence of all the singular basis functions of Table I always gets the same physical $(c_\nu \chi^{\nu-1} - c_0)/\mathcal{J}$ form, with $c_0 = 1$ or 2, and c_ν equal to a constant. As in [4], [12], the divergence of the vector functions belonging to the regular part of the lowest order bases is always equal to $c_0/\mathcal{J}$, with $c_0 = 1$ or 2; for curvilinear elements, this ensures the regular zeroth-order completeness of the divergence with respect to $1/\mathcal{J}$ as a weighting factor.

B. Higher Order Quadrilateral Bases

The $[p, s]$-order bases are obtained by the union of the normalized regular vector set of order p given in [4] with a Meixner set of order s. This latter set

$$\begin{cases} {}^e\mathbf{\Lambda}_{ac;bd}^{i\pm 1}(\boldsymbol{r}) = \alpha_{ac;bd}^{i\pm 1}(s, \boldsymbol{\xi}) \quad {}^e\mathbf{\Lambda}_{i\pm 1}(\boldsymbol{r}) \\ {}^e\mathbf{V}_{ac;bd}^{i+2}(\boldsymbol{r}) = \alpha_{ac;bd}^{i+2}(s, \boldsymbol{\xi}) \quad {}^e\mathbf{V}_{i+2}(\boldsymbol{r}) \end{cases} \tag{18}$$

is obtained by forming the product of the edge singular functions of Table I with the complete Silvester interpolation polynomial factors $\alpha_{ac;bd}^{i\pm 1}(s, \boldsymbol{\xi})$ and $\alpha_{ac;bd}^{i+2}(s, \boldsymbol{\xi})$ reported in [12, Table I]. As explained in [4], the dependency in the regular subset for $p \geq 1$ is easily eliminated by discarding some regular basis functions; the number of degrees of freedom (DOFs) for the regular quadrilateral set is $2(p+1)(p+2)$. Similarly, the dependency of the singular edge functions for $s \geq 1$ is eliminated by discarding all the $s(s+1)$ functions ${}^e\mathbf{\Lambda}_{ac;bd}^{i+1}(\boldsymbol{r})$ for $b = \{1, s\}$; $a, c, d = \{1, s+1\}$, or all the $s(s+1)$ functions ${}^e\mathbf{\Lambda}_{ac;bd}^{i-1}(\boldsymbol{r})$ for $d = \{1, s\}$; $a, b, c = \{1, s+1\}$. Hence, the total number of DOFs per singular quadrilateral is $2(p+1)(p+2) + (s+1)(2s+3)$.

The normal continuity across element boundaries is enforced by adjusting the sign of the edge-based basis functions to correspond to an arbitrarily selected reference direction across adjacent elements.

C. Higher Order Triangular Bases

The $[p, s]$-order bases are obtained by the union of the regular vector set of order p given in [4] with a Meixner set of order s. The Meixner set is either vertex or edge singular, depending on the type of the singularity triangle one considers. These sets are obtained by forming the product of the vertex and edge singular functions given in Table I with the complete Silvester interpolation polynomial factors $\alpha_{abc}^{i\pm 1}(s, \boldsymbol{\xi})$, $\alpha_{abc}^{i}(s, \boldsymbol{\xi})$ reported in [12, Table I]. They can be succinctly written as

$$\begin{cases} {}^\triangleleft\mathbf{\Lambda}_{abc}^{i\pm 1}(\boldsymbol{r}) = \alpha_{abc}^{i\pm 1}(s, \boldsymbol{\xi}) \quad {}^\triangleleft\mathbf{\Lambda}_{i\pm 1}(\boldsymbol{r}) \\ {}^v\mathbf{V}_{abc}^{i}(\boldsymbol{r}) = \alpha_{abc}^{i}(s, \boldsymbol{\xi}) \quad {}^v\mathbf{V}_{i}(\boldsymbol{r}) \end{cases} \tag{19}$$

where the superscript $\triangleleft$ is either equal to e or v according to the type of the singularity triangle at issue. As explained in [4], the dependency in the regular subset for $p \geq 1$ is easily eliminated by discarding some regular basis functions; the number of DOFs for the regular triangular set is $(p+1)(p+3)$. Similarly, the dependency of the singular *vertex* functions for $s \geq 1$ is eliminated by discarding all the $s(s+1)/2$ functions ${}^v\mathbf{V}_{abc}^{i}(\boldsymbol{r})$ for $a = \{1, s\}$; $b, c = \{1, s+1\}$. Hence, the total number of DOFs per vertex singularity triangle is $(p+1)(p+3) + (s+1)(s+3)$.

As far as edge singularity triangles are concerned, all the $(s+1)(s+2)$ basis functions given in the first of (19) are independent because the ghost function ${}^g\mathbf{\Lambda}_i(\boldsymbol{r})$ (and all the functions it generates) has already been eliminated from the lowest order base. Therefore, the total number of DOFs per edge singularity triangle is $(p+1)(p+3) + (s+1)(s+2)$.

Once again, the normal continuity across element boundaries is enforced by adjusting the sign of the edge-based basis functions to correspond to an arbitrarily selected reference direction across adjacent elements.

V. NUMERICAL RESULTS

To illustrate the benefits of singular higher order divergence-conforming vector bases we present several results obtained in the frequency domain by a Galerkin solution of the EFIE for plane wave illumination. The test-cases considered are all relative to zero-thickness PEC-structures in free-space, with wedge aperture angle $\alpha = 0°$; this, with reference to Fig. 2, corresponds to the lowest possible value of the singularity coefficient $\nu = 1/2$, and to the *strongest* singularity. All the test-cases are defined in a cartesian reference frame $\{x, y, z\}$ and were studied by using *regular* bases of higher order $[p]$, as well as by using *singular* bases of $[p, s]$-order containing only one Meixner set; all the elements attached to the edge-profile(s) were considered to be singular when studying the test-cases by use of singular $[p, s]$-order bases.

A. Square Plate

The first test-case is that of a square PEC-plate of zero thickness at normal and at oblique incidence, illuminated by a linearly polarized plane-wave with incident magnetic field of amplitude H^i equal to 1 [A/m] in the y-direction. The side length of the square-plate is equal to one free-space wavelength λ, with top-right and bottom-left corner of the square located at

TABLE II
NUMBER OF UNKNOWNS FOR THE $(1\lambda \times 1\lambda)$ SQUARE PLATE PROBLEM AT NORMAL AND SKEW INCIDENCE

	Normal Incidence		Skew Incidence
Base Order	Mesh A: 636 triangles, with singular bases on 64 vertex singularity and 68 edge singularity triangles	Mesh B: 60 triangles, with singular bases on 14 vertex singularity and 22 edge singularity triangles	Mesh with 240 triangles, and singular bases on 36 vertex singularity and 44 edge singularity triangles
$p = 0$, regular	**920** - used in Figs. 6, 7, 9	**79** - used in Fig. 7	
$p = 0$, $s = 0$	**1116** - used in Fig. 8		
$p = 0$, $s = 2$	**2300** - used in Fig. 8		
$p = 1$, regular		**278** - used in Fig. 7	**1156** - used in Fig. 11
$p = 1$, $s = 0$	**3308** - used in Figs. 7, 8, 9		**1272** - used in Figs. 10, 11
$p = 2$, regular		**597** - used in Figs. 7, 9	
$p = 2$, $s = 0$		**647** - used in Figs. 6, 8, 9	

The number of unknowns is printed in boldface; the figures referenced in the Table were obtained for an incident y-polarized magnetic field $\boldsymbol{H}^i = \hat{\boldsymbol{y}} \ \exp(-j\boldsymbol{k}^i \cdot \boldsymbol{r})$ [A/m], with $\boldsymbol{k}^i = 2\pi\hat{\boldsymbol{z}}/\lambda$ at normal incidence, and $\boldsymbol{k}^i = \pi\left(\hat{\boldsymbol{z}} - \hat{\boldsymbol{x}}\sqrt{3}\right)/\lambda$ at skew incidence. The incident electric field is $\boldsymbol{E}^i = Z_0\,\hat{\boldsymbol{p}}_e \exp(-j\boldsymbol{k}^i \cdot \boldsymbol{r})$ [V/m], with $\hat{\boldsymbol{p}}_e = \hat{\boldsymbol{x}}$ at normal (or $\hat{\boldsymbol{p}}_e = (\hat{\boldsymbol{x}} + \hat{\boldsymbol{z}}\sqrt{3})/2$ at skew) incidence, and where Z_0 is the intrinsic free-space impedance.

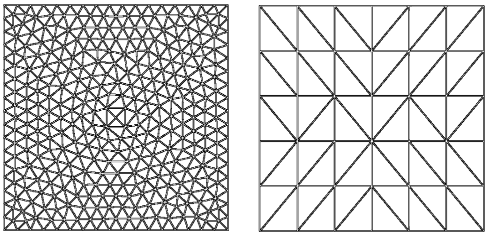
mesh A ***mesh B***

Fig. 5. Triangular meshes for the square PEC-plate problem at normal incidence. The dense mesh (A) consists of 636 triangular elements; the coarse mesh (B) counts 60 triangular elements.

$(x = \lambda/2,\ y = \lambda/2)$ and $(x = -\lambda/2,\ y = -\lambda/2)$, respectively. Table II summarizes the data relative to the meshes used to numerically study this problem, the number of unknowns of the obtained MoM-systems, and the expression of the incident fields at normal and at oblique incidence. Numerical results for the current induced at normal incidence on this same square PEC-plate are reported in [3], [5, ch. 10], [20]; the current density induced at plane-wave incidence on a zero-thickness rectangular PEC-plate with length-to-width ratio equal to 0.7 has been studied in [21] by the method of the Kobayashi potential.

The dense (A) and the coarse (B) triangular meshes we have used to numerically study the square plate problem at normal incidence are shown in Fig. 5, where the horizontal and vertical axes are the x and y axis, respectively. Notice that the length of the largest side of each triangular element of mesh B is roughly equal to 0.2603λ, that is a bit more than $\lambda/4$.

Fig. 6 shows the magnitude of the x-component of the current density (J_x) and the magnitude of the charge density ρ at normal incidence. A 64 color-scale is used to report with a small colored circle the value of the solution at each sampling point of Fig. 6. The sampling points are chosen never to lie on edges or vertices of the triangular elements, where the numerical solution could be discontinuous (across elements' boundaries) or unbounded, as it happens on the sides of the square when singular elements are used. This rendering technique, used also in other figures of this paper, permits one to *recognize* the elements and, above all, does not involve any *fancy* data post-processing which could eventually ameliorate the results, as it happens, for example, when using color-filled contour plots (see for example Fig. 12(c) and (d)). The results at left of Fig. 6 were obtained by using the zeroth-order regular base $[p = 0]$ on the dense mesh A of Fig. 5, thereby solving a problem with 920 unknowns; the results on the right-hand side were obtained by using the coarse mesh B and the singular base of order $[p = 2, s = 0]$, which reduces by 29.67% the number of unknowns and yields to a problem with 647 unknowns. These numbers mean that, on an average, the *density of the unknowns* to obtain the results at left of Fig. 6 is roughly equal to one unknown per square of side-length equal to $\lambda/30$, whereas the density to get the results at right is roughly equal to one unknown per square of side-length equal to $\lambda/25$; in MoM applications, these densities are commonly considered to be very high and are seldom used for far-field analysis, though they are used to obtain good near-field results.

In Fig. 6(b), the (three) brighter spots located along the two vertical sides of the plate in the neighborhood of the singular vertex of the vertex singularity triangles correspond to results of higher value, and are due the poorer modelling capability of the vertex singularity elements discussed in Section III-D. A similar comment holds also for the charge density results of Fig. 6(d) where, along the two horizontal sides of the plate, one can notice some color dribbling from the edge singularity triangles to the vertex singularity triangles attached to them. However, it is rather evident that the quality of the results on the right-hand side of the figure is much better than that of the results on the left-hand side of Fig. 6. In fact, the *color* of each element on the left-hand side of Fig. 6 is almost uniform for the current density results, and completely uniform for the charge density results. In spite of the fact that we used a base with singular order $s = 0$, the solution within the singular elements of Fig. 6(b) and (d) is not uniform in the vicinity of the singular edges, though eventually infinite at these edges. The use of a base with a second order regular part $(p = 2)$ together with the additive nature of our bases made in fact possible to properly model this behavior. As a matter of fact, to improve the quality of the results in the neighborhood of the edge-profile, one does not really need to increase the order s of the singular part of the base, but rather increase the order p of the regular part with s kept equal to zero (see also Fig. 8 and relative discussion). This turns out to be particularly convenient for MoM applications, where the numerical evaluation of the integrals involving bases of singular order $s \geq 1$ is rather delicate because of the presence of a singular Green's function; to avoid numerical problems in MoM applications, we recommend using bases with $s = 0$ if the order p of the regular part of the used base is higher than unity.

The superior modelling capability of our singular divergence-conforming vector bases are better appreciated by considering the normal-incidence results reported in Figs. 7 and 8 which show, for the same square PEC-plate, the magnitude of the x-component of the current density (J_x) along the vertical axis $x = 0$, at left [Figs. 7(a) and 8(a)], and along the horizontal axis $y = 0$, at right [Figs. 7(b) and 8(b)]. In these figures, the reference solution reported by a solid-line was obtained by using mesh A (Fig. 5) and the singular base of order $[p = 1, s = 0]$, thereby solving a problem with 3308 unknowns. Since the numerical results along the considered axes are symmetric with respect to $y = 0$ and $x = 0$, Figs. 7 and 8 show, case by case, the results only over one semi-axis. Fig. 7 reports the results obtained by using the *regular* $[p = 0]$-base on mesh A and B, and the *regular* polynomial vector bases $[p = 1, 2]$ on mesh B. Similarly, Fig. 8 reports the results obtained by using the *singular* vector bases $[p = 0, s = 0, 2]$ with mesh A, and $[p = 2, s = 0]$ with mesh B.

By considering in detail Fig. 7(a), one observes that *regular* bases always yield to non-satisfactory results in the neighborhood of the edge-profile, with solutions that exhibit a non-physical oscillating behavior with (at least) one overshoot in the vicinity of the edge-profile, which becomes rather evident when *higher order regular* bases are used; this phenomenon is well known [5, Ch. 10], [8] and quite similar to the Gibbs' phenomenon observed when expanding in Fourier series periodic functions with a jump discontinuity. Notice also in Fig. 8(a) that the results provided by the *singular* vector bases never suffer for this problem. Fig. 8 further proves that the advantage one gets by increasing the singular order s from $s = 0$ to, say, $s = 2$ is actually negligible even for $p = 0$ (see the Fig. 8 results associated with the negative semi-axes) and, at any rate, certainly not comparable with the big advantage obtained by increasing the order p of the regular part of the base, for s kept equal to zero. Singular higher order divergence-conforming bases with $s \geq 2$ can be used for the numerical solution of integral equations provided the MoM potential and testing integrals are evaluated with a very high degree of accuracy; this, at present, is very expensive and would require large computational times. The potential advantage of using bases with $s \geq 2$ is only related to the possibility of obtaining solutions which are *almost* continuous on the edges of the singular elements also in the direction tangent to these edges; the divergence-conforming nature of our bases already guarantees the continuity of the normal component of the vector unknown across the element edges. The fact that higher order divergence-conforming bases eventually yield to solutions with tangent component *almost* continuous on the element edges should be evident by considering the *dual* case of application of higher order curl-conforming functions to the finite element (FE) solution of partial differential equations [12], [22]; under the numerical point of view, these FE applications are much simpler than the present one because they do not require numerical integration of a singular Green's function. A technique for machine precision evaluation of potential integrals involving singular Green's kernels and higher order regular basis functions has been recently presented in [23].

Since our singular bases improve the quality of the numerical results in the wedge near-field region (indeed they were derived to that purpose), the reader may wonder if they have also some beneficial effect on the far-field results with respect to the case when one uses regular bases only. These effects are in general expected to be negligible in the far-field because: a) the radiation integral-operator cuts off the highest spatial-frequency components of the charge and current densities arising from the singular behavior of these quantities in the wedge neighborhood; b) the MoM-Galerkin method used to approximately evaluate the surface charge and current densities is variational (see [24, Ch. 1.8], [25], [38] and references therein). At any rate, in the attempt to quantitatively clarify these effects, Fig. 9 shows few bistatic results for the electric field scattered in the far-field region by the zero-thickness square PEC-plate at normal incidence. Numerical results for the bistatic scattering from thin square plates one wavelength on a side are available in [26]. In Fig. 9, a spherical reference frame $\{r, \theta, \phi\}$ centered at $(x, y, z) = (0, 0, 0)$ is understood, with $\hat{\boldsymbol{r}} = \hat{\boldsymbol{z}}$ at $\theta = 0°$ while, for $\theta = 90°$, one gets $\hat{\boldsymbol{r}} = \hat{\boldsymbol{x}}, \hat{\boldsymbol{y}}$ at $\phi = 0°$ and $90°$, respectively. Fig. 9(a) shows the bistatic radar cross sections $\sigma_\phi(\theta, \phi = 90°)$ and $\sigma_\theta(\theta, \phi = 0°)$ at normal incidence in the principal plane $x = 0$ and $y = 0$, respectively, with

$$\sigma_{\phi,\theta}(\theta, \phi) = \lim_{r \to \infty} 4\pi r^2 \frac{|E^s_{\phi,\theta}|^2}{|\boldsymbol{E}^i|^2} \tag{20}$$

and where, in our case, $\boldsymbol{E}^i$ is x-directed (see Table II). These radar cross section results were normalized w.r.t. the area of the plate (λ^2), and agree with the results available in the literature (see for example [27], [28] and references therein). Fig. 9(b) and (c) reports the relative error of the far-scattered field components E_ϕ and E_θ in the principal plane $x = 0$ and $y = 0$, respectively. The reference solution to evaluate these errors is the one obtained by using the singular base of order $[p = 1,\ s = 0]$ on the dense mesh of Fig. 5 (3308 unknowns). In the two considered principal planes, in the forward $(\theta = 0°)$ and backward $(\theta = 180°)$ scattering direction, the E_θ and E_ϕ components are relative to the same scattered electric field vector; this is why in the figure one has $\sigma_\phi = \sigma_\theta$ (and $|E_\theta| = |E_\phi|$) at $\theta = 0°, 180°$. Although in this PEC-plate case the far-field error obtained by using the regular base of order $[p = 0]$ (with dense Mesh A-920 unknowns) and $[p = 2]$ (with coarse mesh B-597 unknowns) is less than 1%, the error is still numerically detectable and at least three times higher than the error due to the use of the singular $[p = 2, s = 0]$-order base on the coarse mesh B (647

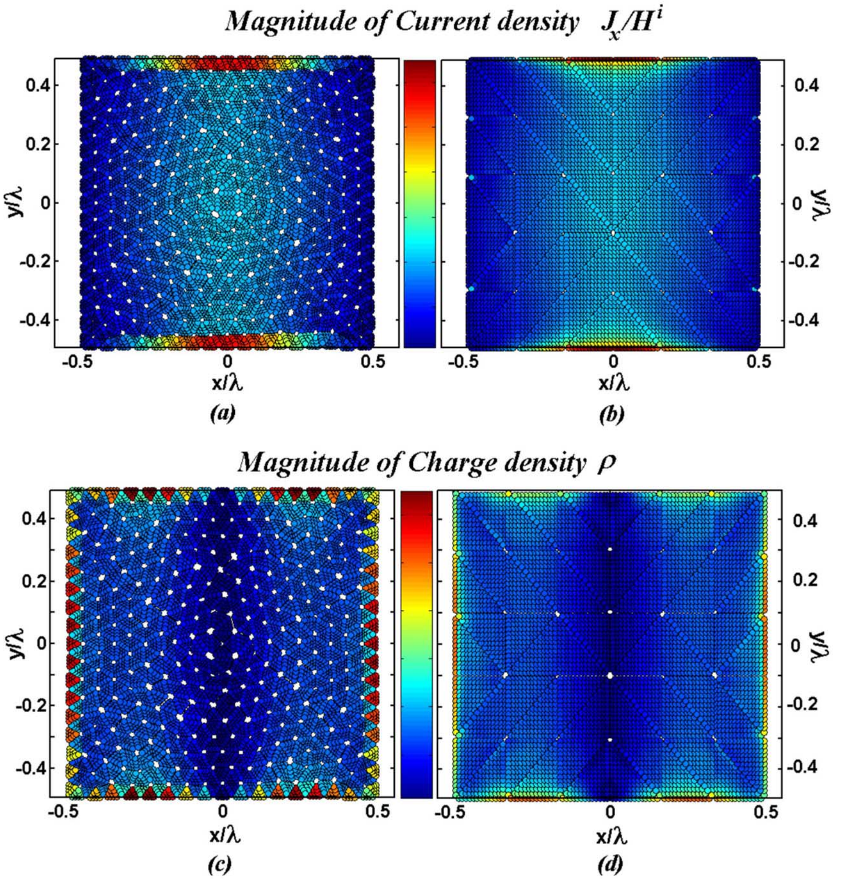

Fig. 6. A zero-thickness square PEC-plate at normal incidence. The incident field and the number of unknowns are specified in Table II. The magnitude of the current density in the x-direction (a), (b), and of the charge density (c), (d), normalized w.r.t. H^i, are reported by using a 64 color-scale. The maximum value (dark-red) of the scale used for the normalized current and for the normalized charge density is 8.73 and 3.615, respectively. The results at left (a), (c) were obtained by using the zeroth-order regular base $(p = 0)$ on the dense mesh A of Fig. 5. The results at right (b), (d) were obtained by using the coarse mesh B and the singular base of order $[p = 2, s = 0]$.

unknowns). Notice also in Fig. 9(b) and (c) the regular pattern of the error as a function of θ; the error diminishes by increasing the order of the used regular base and is minimum for the singular $[p = 2, s = 0]$-order base. Although the error in the far-field region due to the use of *regular* (high order) bases is usually neglected, there are applications where this error is of some importance.

Figs. 10 and 11 report the current induced at skew incidence on the same square PEC-plate previously considered at normal incidence. In this case, the angle between the incident propagation unit vector $\hat{\boldsymbol{k}}^i = (\hat{\boldsymbol{z}} - \sqrt{3}\hat{\boldsymbol{x}})/2$ and the $\hat{\boldsymbol{z}}$ unit-vector is 60°, with incident magnetic field of amplitude H^i equal to 1 [A/m] again polarized in the y-direction (see Table II); the phase of the incident $\boldsymbol{E}^i$ and $\boldsymbol{H}^i$ field is zero along $x = 0$. The triangular mesh used to solve this problem (240 elements) is recognizable in Fig. 10, which reports the magnitude (at left) and phase (at right) of the induced current component J_x. The largest side of each triangular element is roughly equal to 0.13λ, that is a bit more than $\lambda/8$. At this skew incidence, the induced current exhibits two hot zones on the upper and lower edge whereas, at normal incidence (Fig. 6), only one hot zone is present along these edges. Fig. 11 shows the behavior of the phase of J_x along four different line-cuts of the square-plate. In particular, Fig. 11(a) shows results obtained by using the *regular* base of order $[p = 1]$ (1156 unknowns), whereas Fig. 11(b) reports results obtained by using the *singular* base of order $[p = 1, s = 0]$ (1272 unknowns). From this figure one can readily observe that, in the vicinity of the edge-profile, the use of regular bases spoils also the phase results (the fact that *regular* bases spoils the magnitude results was put on evidence while discussing Figs. 7 and 8); in fact, by using regular elements, the phase exhibits non-physical peaks in the vicinity of the upper and lower side of the square-plate [see Fig. 11(a)]; conversely, the phase results provided by singular bases do not suffer for this problem. It is also interesting to notice that the phase of the induced current J_x is not zero along the $x = 0$ line, while the phase of the incident field is zero over there.

B. Long Narrow Strip

The second test-case considers a rectangular $(10\lambda \times 1\lambda)$ PEC-strip of zero thickness at normal incidence illuminated, as specified in Table III, by a linearly polarized plane-wave with incident electric field in the x-direction, and incident magnetic field of amplitude H^i equal to 1 [A/m] in the y-direction. The top-right and bottom-left corner of the PEC-plate are at $(x = 5\lambda, y = \lambda/2)$ and $(x = -5\lambda, y = -\lambda/2)$, respectively.

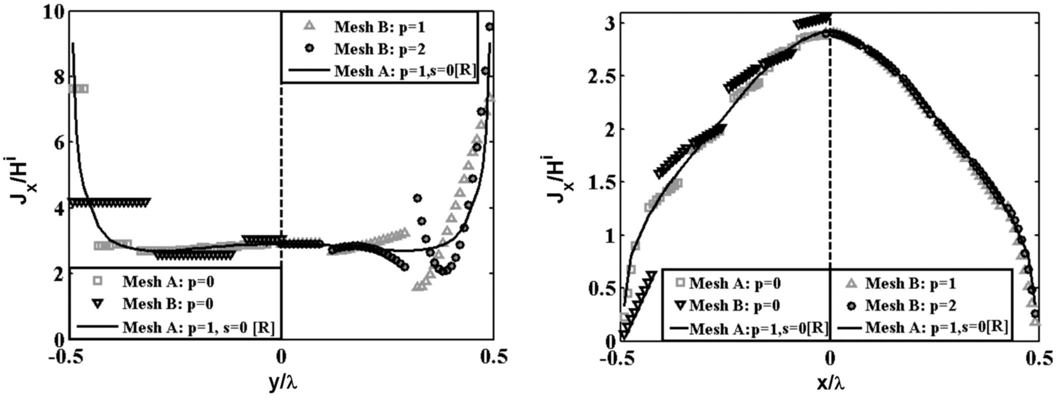

(a) (b)

Fig. 7. Normalized magnitude of the current component J_x on a $(1\lambda \times 1\lambda)$ square PEC-plate at normal incidence: (a) along the vertical axis $x = 0$; (b) along the horizontal axis $y = 0$. The incident plane-wave is the same considered in Fig. 6. The results, computed by using *regular* vector bases of order $p = 0$, 1, and 2, are reported only over a semi-axis because of their symmetry with respect to $y = 0$ and $x = 0$. The reference solution (solid-line) was obtained with mesh A (Fig. 5) by using the singular base of order [1, 0].

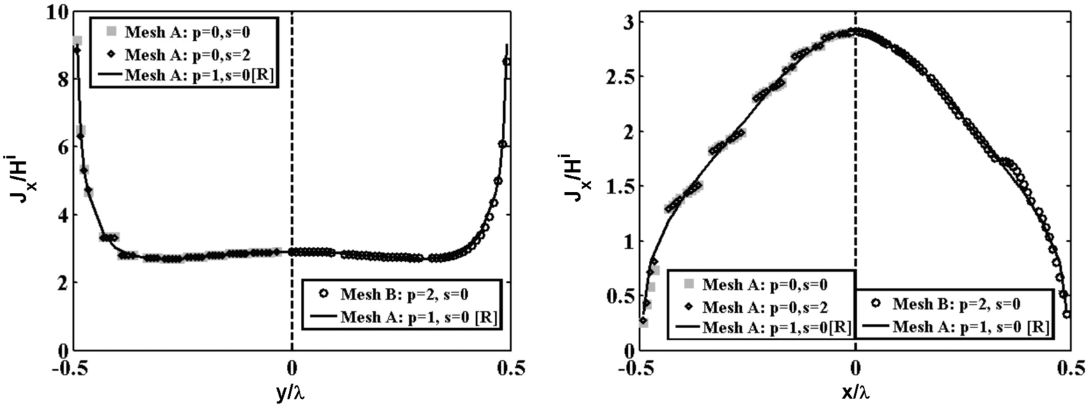

(a) (b)

Fig. 8. Normalized magnitude of the current component J_x on a $(1\lambda \times 1\lambda)$ square PEC-plate at normal incidence: (a) along the vertical axis $x = 0$, (b) along the horizontal axis $y = 0$. The incident plane-wave is the same considered in Fig. 6. The results, computed by using *singular* vector bases of order [0, 0], [0, 2], and [2, 0], are reported only over a semi-axis because of their symmetry with respect to $y = 0$ and $x = 0$. The reference solution (solid-line) was obtained with mesh A (Fig. 5) by using the singular base of order [1, 0].

The mesh used to numerically study this case counts 266 triangular elements and is shown in Fig. 12(a), where the horizontal and vertical axes are the x and y axis, respectively. Although not completely evident at glance, the mesh used in this case is rather coarse because, for the great majority of the used elements, the length of each side of the triangles is comprised between $\lambda/4$ and $\lambda/3$. This structure has then been modelled by using the $[p = 2, s = 0]$ singular base on the mesh of Fig. 12(a), thereby solving a problem with 2885 unknowns. This means that, on an average, the *density of the unknowns* is slightly less than one unknown per square of side-length equal to $\lambda/17$, which is a density adequate to guarantee good numerical results in the near-field region, also because the order of the regular part of the used base is $[p = 2]$.

The results of Fig. 12(b) and (c) show the magnitude of the x-component of the current density (J_x) by using a 64 color-scale. The maximum value (dark-red) of the scale used to represent the current is 4.38; this rather low value is due to the fact that we never sampled the results in the close vicinity of the edge-profile. The current in the neighborhood of the edge profile is unbounded and by choosing samples more close to the edge-profile one eventually looses the possibility to show the dynamic of the results in the interior of the strip. Fig. 12(c) is the color-filled contour plot of the same results shown in Fig. 12(b), whereas Fig. 12(d) is zooming on the region bounded by the black-frame of Fig. 12(c). A quantitative representation of the strip results is provided in Fig. 13, which reports the magnitude of J_x along different vertical [Fig. 13(a)] and horizontal [Fig. 13(b)] axes individuated by different values of the x and y coordinates, respectively.

It is instructive to note in Fig. 12(c) and Fig. 13(b) the pseudo-periodicity of the results along the x-axis, with a pseudo-period equal to 1λ. This test-case was considered also in [11] although, in there, the pseudo-periodicity of the results was not pointed out.

C. Circular Plate

The scattering from a circular disk is a problem amenable to a wide variety of analytical treatments and it was extensively studied in the literature. Historically, the first results were derived by using Babinet's principle to convert the circular aperture results into the appropriate results for the disk [29].

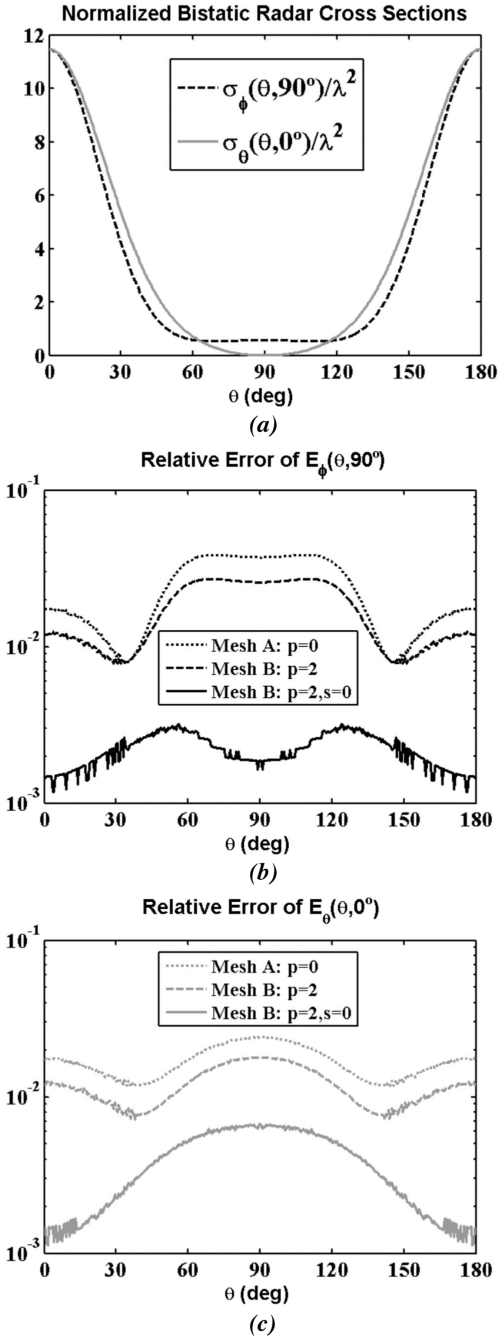

Fig. 9. Far-field scattered by a square PEC-plate at normal incidence: (a) normalized RCS σ_θ and σ_ϕ in the principal plane $y = 0$ and $x = 0$, respectively, (b) relative error for the E_ϕ component in the principal plane $x = 0$, (c) relative error for the E_θ component in the principal plane $y = 0$. The incident wave is the same of Fig. 6, with forward and backward directions corresponding to $\theta = 0°$, $180°$, respectively. The reference solution to evaluate the errors was obtained by using the $[p = 1, s = 0]$ singular base on the dense mesh of Fig. 5.

For plane wave incidence, several far-field scattering results are readily available in [29], together with typical results for the surface current density induced on the disk. Numerical estimates of the surface current components induced on a thick disk at grazing incidence are available in [30], whereas scattering results in the disk far-field region are available in numerous papers (see for example [30]–[35] and references therein). MoM-results for the current induced on a circular disk at plane-wave incidence are reported in [34].

Because of the importance of this problem, and in order to show that our singular bases can be used on curved elements, we consider, as a third-test case, a zero-thickness circular PEC-plate with diameter equal to one wavelength λ. The plate is illuminated by a linearly polarized plane-wave with incident electric field in the x-direction, and incident magnetic field of amplitude H^i equal to 1 [A/m] in the y-direction. The mesh used for this problem, readily recognizable in Fig. 14, counts 64 (quadratic curvilinear) triangular elements. The problem was discretized by using the regular $[p = 2]$ base and the singular $[p = 2, s = 0]$ base which yield to 648 and 696 unknowns, respectively (see Table III). In both cases, the number of unknowns corresponds, on an average, to a very high *density of the unknowns*, roughly equal to one unknown per square of side-length equal to $\lambda/29$, which one would expect to guarantee extremely accurate numerical results in the near-field region.

Fig. 14 reports colored results for the current and charge density obtained with the singular $[p = 2, s = 0]$ base. The quantitative results given in Fig. 15 for the circular PEC-plate show the magnitude of the x-component of the current density (J_x) along the vertical $(x = 0)$ axis [Fig. 15(a)], and along the horizontal $(y = 0)$ axis [Fig. 15(b)]. Along the vertical-axis, J_x is the azimuthal current-component whereas, along the horizontal axis, it corresponds to the radial current-component. The results for the charge density along the horizontal $(y = 0)$ axis are reported in Fig. 16. Figs. 15, 16 report also the results for the regular $[p = 2]$ base to show, once more, that *regular* bases yield to solutions with non-physical oscillating behavior in the vicinity of the edge-profile.

Among the text-case problems considered in this paper, the PEC circular disk at plane-wave incidence is the only one with available and well established analytical solutions. Although these solutions usually involve rather complex series expansions in terms of oblate spheroidal wave functions, a simple and very accurate low frequency approximation for the singular surface current density induced on an infinitely thin disk at normal incidence has been obtained by Bouwkamp and published in 1950 [36] (see also [29]). The truncated series expression obtained by Bouwkamp for the disk current density $\boldsymbol{J}_B$ has been used to evaluate the convergence of our numerical solutions to the exact one by studying the relative error

$$\mathrm{Err} = \frac{\int\int_{\mathrm{disk}} |\boldsymbol{J}_{\mathrm{MoM}} - \boldsymbol{J}_B| \mathrm{d}S}{\int\int_{\mathrm{disk}} |\boldsymbol{J}_B| \mathrm{d}S} \tag{21}$$

for the MoM-computed current $\boldsymbol{J}_{\mathrm{MoM}}$. Notice here that the relative current error (21) is defined differently from what usually done when dealing with smooth scatterers, where one can define and use the L^2 current error because of the boundedness of the induced surface current, which is always square integrable whenever the electromagnetic sources do not lie on the smooth-scatterer surface [13]. In the present case, the current density on the infinitely thin disk is not bounded and not square-integrable, since the singularity factor ν is equal to 1/2. The Bouwkamp truncated series for $\boldsymbol{J}_B$ has an error of the order $(\pi d/\lambda)^7$, d and λ being the disk diameter and the free-space wavelength, respectively. In order to consider the Bouwkamp result as a reference, we numerically studied the induced

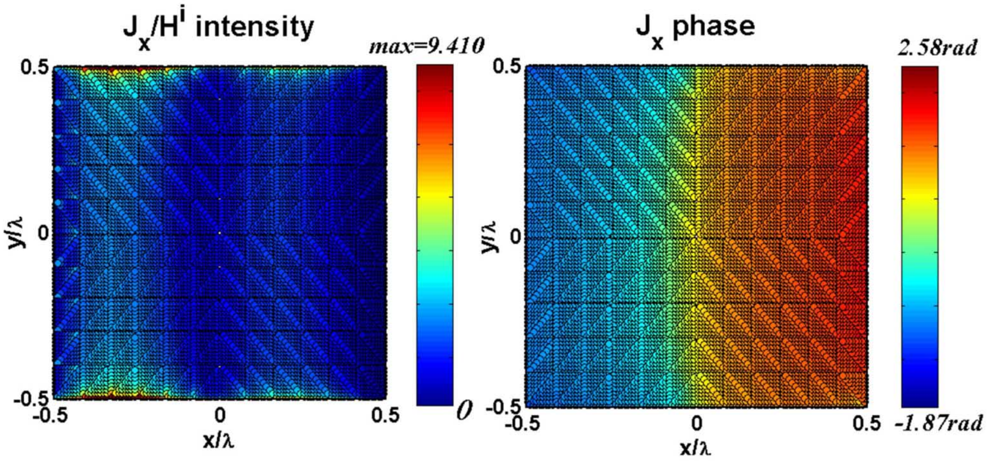

(a) (b)

Fig. 10. Normalized magnitude (a) and phase (b) of the current density in the x-direction induced on a $(1\lambda \times 1\lambda)$ PEC-plate of zero thickness at skew incidence (see Table II). The solution has been obtained with a 240 triangular element mesh, easily recognizable in the figure, by using the singular base of order $[p = 1, s = 0]$, thereby solving a problem with 1272 unknowns.

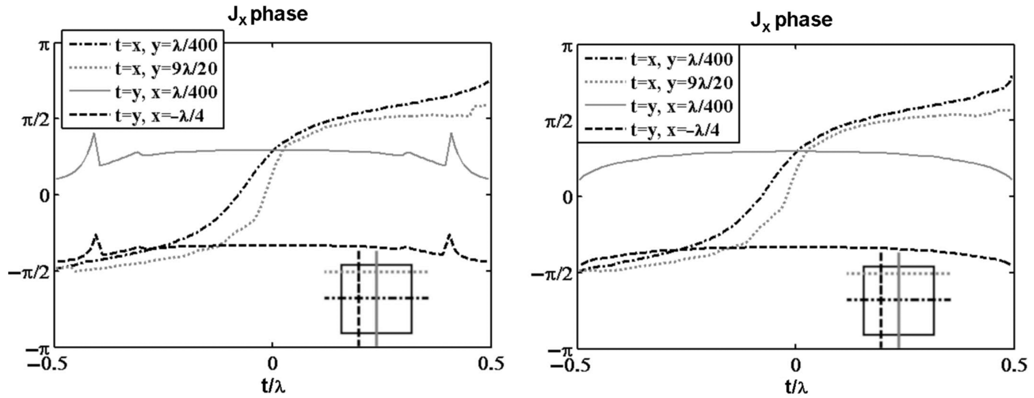

(a) (b)

Fig. 11. Phase of the current density J_x induced on a $(1\lambda \times 1\lambda)$ PEC-plate of zero thickness at skew incidence. The incident plane-wave is the same of Fig. 10. The figure reports the phase behavior along four line-cuts of the square-plate, schematically represented in the insets. The results were obtained with the same mesh of Fig. 10 by using: (a) the regular base of order $[p = 1]$; (b) the singular base of order $[p = 1, s = 0]$.

current density on a disk of diameter $d = \lambda/100$, thereby proving, although indirectly, that our code does not breakdown in the low-frequency limit.

In Fig. 17 we compare the relative current error results obtained by using regular vector functions of order $p = 0$, 1, and 2 with those obtained by using singular vector functions of order $[p = 0, s = 0]$ and $[p = 1, s = 0]$. The results were obtained with five different meshes made with 32, 64, 256, 512, and 1024 quadratic curvilinear triangular elements. The number of the degrees of freedom (that is, the dimension of the MoM system matrix) relative to the use of the regular bases ranges from 40 (when using the $p = 0$ base on the 32 element mesh) to 5304 (when using the $p = 2$ base on the 512 element mesh); the numerical problem has 1504 unknowns for the $p = 0$ base on the 1024 element mesh. The number of the degrees of freedom relative to the use of the singular bases ranges from 72 (when using the $[p = 0, s = 0]$ base on the 32 element mesh) to 2656 (when using the $[p = 1, s = 0]$ base on the 512 element mesh); the numerical problem has 1728 unknowns for the $[p = 0, s = 0]$ base on the 1024 element mesh.

The results of Fig. 17 show that the error obtained by using regular vector functions weakly improves by increasing the order of the expansion functions. Conversely, when singular functions are included in the numerical model, the relative current error considerably diminishes and the rate of convergence of the numerical results improves for increasing order of the regular part of the bases. Notice however that the errors obtained by using the singular bases for the coarse 32-element mesh are worse than what *expected* by following the relevant *slope-lines* because of the poor geometrical modelling of the rim of the disk, that is of the region where the current density goes to infinity. Finally we remark that, to the best of our knowledge, no result (or estimate) is available in the open literature for the *current* error on 3D-structures with edges [13].

D. Square Plate With an Offset Circular Hole

The fourth test-case is relative to the square PEC-plate already considered in Figs. 5–8 but, this time, the plate has a circular hole of radius $r = \lambda/10$ centered at

TABLE III
NUMBER OF UNKNOWNS FOR THE TEST PROBLEMS 2, 3, AND 4 AT NORMAL INCIDENCE

	$(10\lambda \times 1\lambda)$ - Strip	Circular Plate (1λ in diameter)	$(1\lambda \times 1\lambda)$ - Square Plate with an Offset Circular Hole ($\lambda/10$ in radius)
Base Order	Meshed with 266 triangles, with singular bases on 64 vertex singularity and 72 edge singularity triangles	Meshed with 64 triangles, with singular bases on 16 vertex singularity and 16 edge singularity triangles	Meshed with 128 triangles, with singular bases on 28 vertex singularity and 26 edge singularity triangles
$p = 1$, regular			**614** - used in Fig. 18
$p = 1, s = 0$			**696** - used in Fig. 18
$p = 2$, regular		**648** - used in Figs. 15, 16	
$p = 2, s = 0$	**2885** - used in Figs. 12, 13	**696** - used in Figs. 14, 15, 16	

The number of unknowns is printed in boldface; the figures referenced in the Table were obtained for an incident y-polarized magnetic field $\boldsymbol{H}^i = \hat{\boldsymbol{y}}\ \exp(-j\boldsymbol{k}^i \cdot \boldsymbol{r})$ [A/m], and an incident electric field $\boldsymbol{E}^i = Z_0\,\hat{\boldsymbol{x}}\,\exp(-j\boldsymbol{k}^i \cdot \boldsymbol{r})$ [V/m], with $\boldsymbol{k}^i = 2\pi\hat{\boldsymbol{z}}/\lambda$, and where Z_0 is the intrinsic free-space impedance.

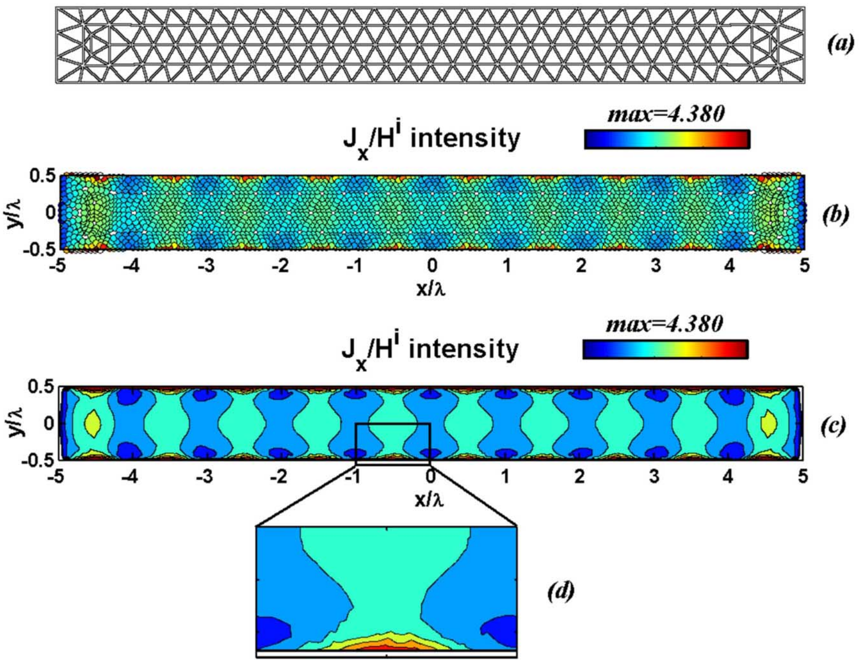

Fig. 12. A $(10\lambda \times 1\lambda)$ PEC-strip normally illuminated by a linearly polarized plane-wave with incident electric field in the x-direction, and incident magnetic field in the y-direction. (a) Triangular mesh; (b, c) normalized magnitude of the current density J_x in the x-direction computed by using the singular base $[p = 2, s = 0]$ (see also Table III); (d) normalized magnitude of J_x in the region bounded by the black-frame shown in Fig. 12(c).

$(x = -0.15\lambda, y = +0.15\lambda)$. The structure is numerically described by the 128 (quadratic curvilinear) triangular element mesh given in Fig. 18(a), which contains six couples of vertex-singularity triangles with a common singular vertex on the hole-rim. The perforated plate is normally illuminated by a linearly polarized plane-wave with incident electric field in the x-direction, and incident magnetic field of amplitude H^i equal to 1 [A/m] in the y-direction. Fig. 18(b) and (c) show the magnitude of the charge and current density, respectively. These results have been obtained by the singular base of order $[p = 1, s = 0]$, thereby solving a problem with 696 unknowns (recall that the results of Fig. 6(b) and (d) for the *solid* plate problem were obtained by solving a problem with 647 unknowns). Fig. 18(d) quantitatively compares, along the $x = -0.15\lambda$ axis, the results for the magnitude of the x-component of the current density obtained by the singular base with those obtained by using the regular base of order $[p = 1]$ (614 unknowns). Once again, the results of Fig. 18(d) prove the superior modelling capabilities of our singular bases with respect to those of regular higher order vector bases.

E. Sphere With Aperture

The last test-case is the same one described in [11, Fig. 5], [37] and considers an infinitely thin, spherical PEC-shell with an aperture angle (measured from the sphere center) $\theta_0 = 120°$. The sphere center is at $(x, y, z) = (0, 0, 0)$. The radius a of the spherical surface is equal to $\lambda/(2\pi)$ (that is, $ka = 1$; $a \simeq 0.1591\lambda$) and the negative z-axis passes through the center of the aperture, which lies in the plane $z = -a/2$ and has a circular rim of radius $r = a\sqrt{3}/2 \simeq 0.1378\lambda$. The PEC-surface is illuminated by a plane-wave propagating in the positive $\hat{\boldsymbol{z}}$ direction with vector wavenumber $\boldsymbol{k}^i = 2\pi\hat{\boldsymbol{z}}/\lambda$, and incident field $\boldsymbol{H}^i = \hat{\boldsymbol{y}}\exp(-j\boldsymbol{k}^i \cdot \boldsymbol{r})$ [A/m], $\boldsymbol{E}^i = Z_0\hat{\boldsymbol{x}}\exp(-j\boldsymbol{k}^i \cdot \boldsymbol{r})$ [V/m], Z_0 being the intrinsic free-space impedance. Fig. 19 shows the

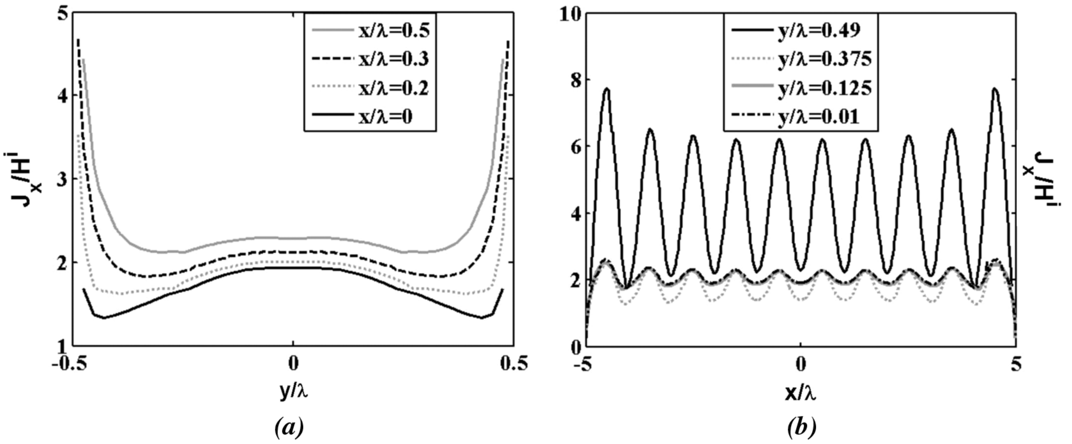

Fig. 13. Normalized magnitude of the current density J_x induced at normal incidence on a $(10\lambda \times 1\lambda)$ PEC-strip: (a) along the vertical axes located at the different values of the x-coordinate reported in the inset and (b) along the horizontal axes individuated by the different values of the y-coordinate given in the inset. The incident plane-wave is the same of Fig. 12.

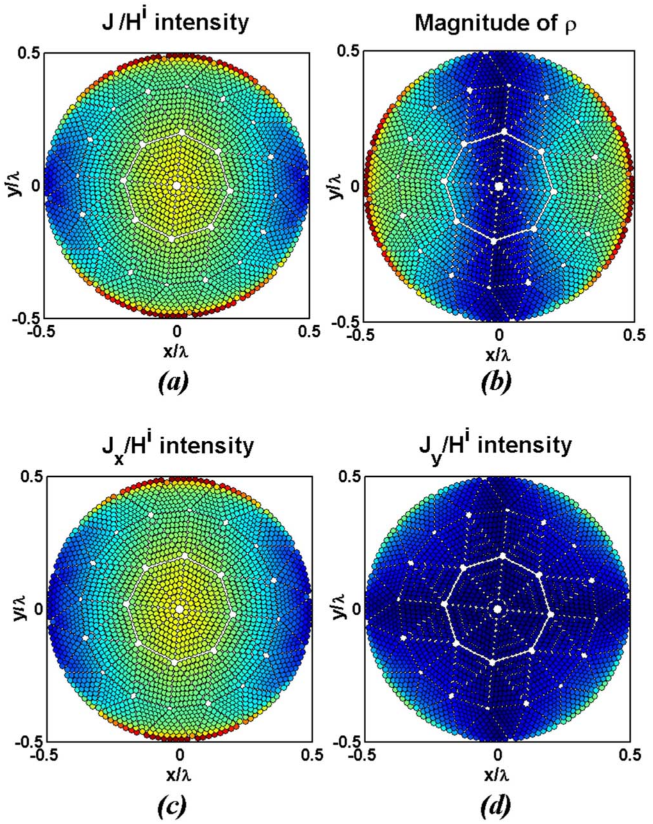

Fig. 14. Normal incidence on a circular PEC-plate (1λ in diameter). The results were obtained by using the $[p = 2, s = 0]$ base on a 64 triangular element mesh (see Table III). Normalized magnitude (w.r.t. H^i) of: (a) the total current density, (b) the charge density, (c) x-component, (d) y-component of the current density. A 64 color-scale is used, and the maximum value (dark-red) of the scale for the normalized current and charge densities is 5.0799 and 2.2765, respectively.

magnitude of the total current induced on the spherical-shell by using a 64 color-scale where this time, for rendering purposes, the used color-scale is logarithmic. In fact, the magnitude of the current in the vicinity of the aperture rim is so high that only the logarithmic scale permits one to distinguish the difference in the current out of the rim. Two different views of the illuminated structure are shown in Fig. 19, which reports the results obtained by modelling the shell-surface with 30 quadratic curvilinear triangles on which we used the singular $[p = 2, s = 0]$-order base. In this case, our MoM systems has 328 unknowns (with a *density of the unknowns* roughly equal, on an average, to one unknown per square of side-length equal to $\lambda/37$), while 636 unknowns were used to solve the same problem in [11] with non-additive basis functions of zeroth-order that incorporate the edge conditions.

In Fig. 20, a spherical reference frame $\{r, \theta, \phi\}$ centered at $(x, y, z) = (0, 0, 0)$ is understood, with $\hat{\boldsymbol{r}} = \hat{\boldsymbol{z}}$ at $\theta = 0^\circ$, and $\hat{\boldsymbol{r}} = \hat{\boldsymbol{x}}$ at $(\theta, \phi) = (90^\circ, 0^\circ)$. The $\hat{\phi}$ directed current at $\phi = 90^\circ$ is reported in Fig. 20(a), while the results in Fig. 20(b) show the $\hat{\theta}$ directed current at $\phi = 0^\circ$. Fig. 20 reports also the results obtained by using the regular $[p = 2]$-order base on the same mesh of Fig. 19, which yields to a MoM system with 306 unknowns. The *wiggly* behavior of the results for the $\hat{\theta}$-directed current around the point $\theta \simeq 100^\circ$, $\phi = 0^\circ$ [Fig. 20(b)] is due to the fact that, in the vicinity of this shell point, the 30-elements mesh of Fig. 19 has a vertex-point in common to five different triangular elements, two of which are vertex singular triangles.

To further clarify the modelling problems encountered in dealing with wedge structures by using regular vector bases, Fig. 20 reports also the results obtained with the regular zeroth-order base on a very dense mesh (1056 quadratic curvilinear triangles, 1564 unknowns, with a *density of the unknowns* roughly equal, on an average, to one unknown per square of side-length equal to $\lambda/81$). Once again notice how regular bases badly model the singularity of the current; in fact, in Fig. 20(a), the regular bases results oscillate in the range $\{85^\circ \lesssim \theta \lesssim 115^\circ\}$, and are always in error for $\theta \gtrsim 110^\circ$. Furthermore, in Fig. 20(b), the results provided by use of the zeroth-order regular base on the dense (1056 elements) mesh are quite unsatisfactory for $\{85^\circ \leq \theta \leq 115^\circ\}$; in this wide-range these results seldom coincide with those obtained by using the singular $[p = 2, s = 0]$-base and, when this happens, it occurs only at specific θ values, never on a range of values.

VI. CONCLUSION

New subsectional, singular divergence-conforming vector bases that incorporate the edge conditions for conducting

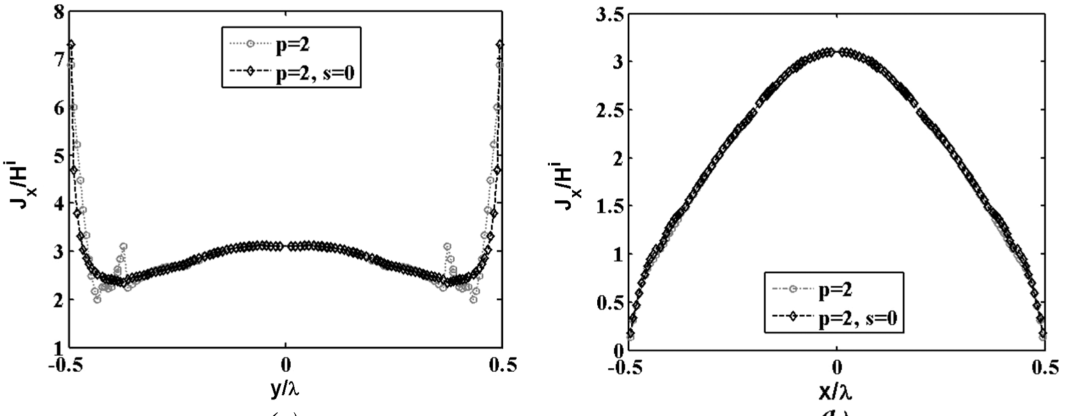

(a) (b)

Fig. 15. Normal incidence on a circular PEC-plate of diameter equal to 1λ. The incident plane-wave is the same of Fig. 14. The results were computed by using the regular vector base of order $p = 2$, and the singular base of order [2, 0]. Normalized magnitude of the current component J_x: (a) along the vertical axis $x = 0$, and (b) along the horizontal axis $y = 0$.

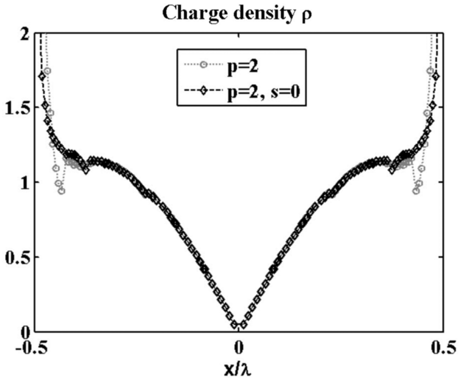

Fig. 16. Normalized magnitude (w.r.t. to H^i) of the charge density ρ along the vertical axis $x = 0$ of a circular PEC-plate of diameter equal to 1λ. The normally incident plane-wave is the same of Fig. 14. The results were computed by using the regular vector base of order $p = 2$, and the singular base of order [2, 0].

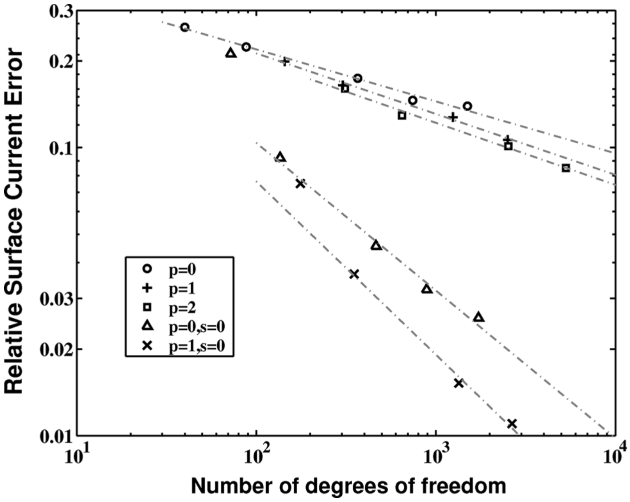

Fig. 17. Relative surface current error for a infinitely thin disk of diameter $d = \lambda/100$ at normal incidence as a function of the used number of unknowns (number of degrees of freedom). The order of the used expansion functions is reported in the inset.

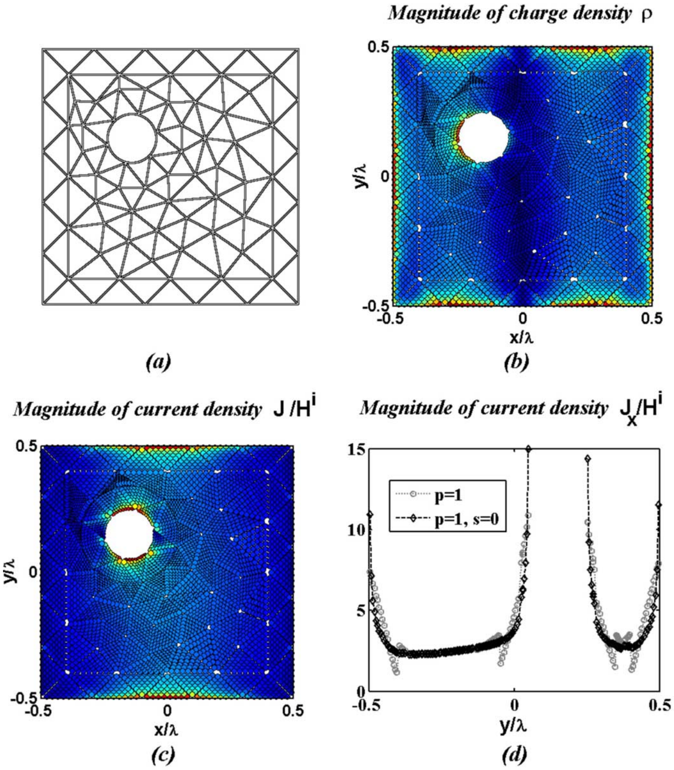

Fig. 18. Normal incidence on a $(1\lambda \times 1\lambda)$ square PEC-plate with a hole of radius $r = \lambda/10$ centered at $(x = -0.15\lambda, y = +0.15\lambda)$; the incident magnetic field is polarized in the y-direction. (a) Triangular mesh (see Table III), (b) normalized magnitude (w.r.t. H^i) of the charge density, (c) normalized magnitude of the total current density, (d) normalized magnitude of the x-component of the current density along the $x = -0.15\lambda$ axis. The maximum value (dark-red) of the color-scale used for the normalized charge (b) and current (c) density is 3.301 and 10.940, respectively.

wedges are developed. The bases for curved quadrilateral and triangular elements are obtained by incrementing the regular polynomial vector bases with other subsectional basis-sets that model the singular behavior of the unknown vector field in the wedge neighborhood. The *additive nature* of our bases permits one to deal with all cases where the singularity of the fields is not excited and does not require one to limit the size of the mesh in the neighborhood of the edge of the wedge. The regular part of our bases can also model the nonsingular divergence-less part of the current component normal to the edge of the wedge, whenever this current is present.

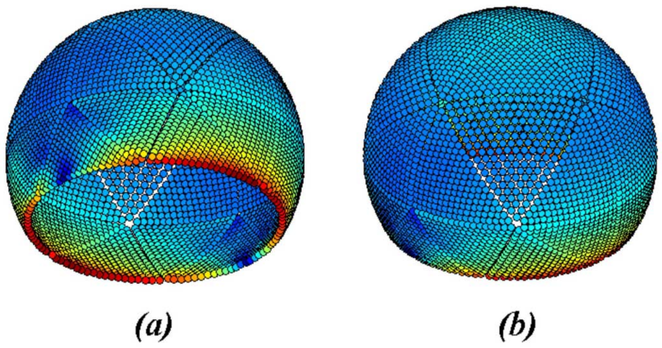

Fig. 19. A spherical PEC-shell of radius $a = \lambda/(2\pi)$ and aperture angle $\theta_0 = 120^\circ$ is illuminated by a plane-wave propagating in the positive $\hat{\boldsymbol{z}}$ direction. The sphere center is at $(x, y, z) = (0, 0, 0)$. The negative z-axis passes through the center of the aperture, which lies in the plane $z = -a/2$ and has a circular rim of radius $r = a\sqrt{3}/2$. By using a logarithmic 64-color scale, the figure shows the magnitude of the total current induced on the shell seen from two different points of view: $(\theta, \phi) = (117^\circ 56' 18'', 45^\circ)$ at left, and $(\theta, \phi) = (60^\circ, 52^\circ 30')$ at right. The hidden part of the shell was not removed from the figures, and brighter results relative to the hidden part of the shell shine through the blue triangle located in the middle of (b).

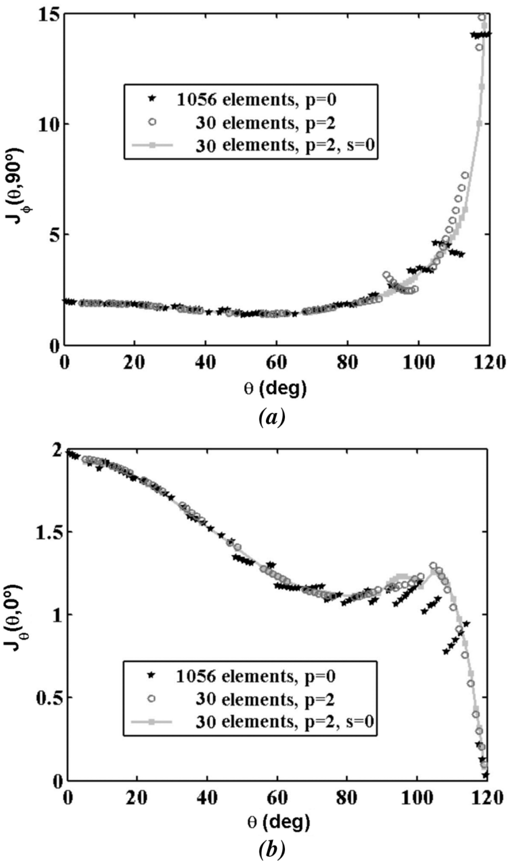

Fig. 20. Normalized magnitude (w.r.t. H^i) of the currents induced on the spherical PEC-shell of Fig. 19 as function of the angle θ (in degrees). (a) The singular $\hat{\phi}$ directed current at $\phi = 90^\circ$, (b) $\hat{\theta}$ directed current at $\phi = 0^\circ$. The figure reports the results obtained by using the regular $[p = 2]$-order base (306 unknowns) and the singular $[p = 2, s = 0]$-order base (328 unknowns) on the same 30-elements mesh of Fig. 19. The results obtained with the regular zeroth-order base on a very dense quadratic curvilinear triangular mesh (1056 elements, 1564 unknowns) are reported to further clarify the modelling problems encountered in dealing with wedge structures by use of regular vector bases.

Singular bases of this kind, complete to arbitrarily high order, are then described in a unified and consistent manner. The higher order basis functions are obtained as the product of lowest order functions and Silvester-Lagrange interpolatory polynomials with specially arranged arrays of interpolation points. The completeness properties of our bases are discussed by first deriving and then considering a generalized expression of the Meixner approximation that deals with curved edge-profile. The bases are also proved to be fully compatible with the standard, high-order regular vector bases used in adjacent elements. Our singular bases guarantee normal continuity along the edges of the elements allowing for the discontinuity of tangential components, adequate modelling of the divergence, and removal of spurious solutions. The paper considers several 3D wedge-structures as test-cases, thereby obtaining highly accurate numerical results for the current and charge density induced on these structures. The results are compared with other solutions, when available, and confirm the faster convergence of these new bases on wedge problems.

APPENDIX I
SHARP-EDGE POTENTIALS FOR SINGULAR DIVERGENCE-CONFORMING BASES

The singular edge-based vector functions given in [11] were derived by integrating a surface divergence with the correct singular behavior, to later impose the continuity of the normal component along one of the element edges and the vanishing of the normal component along the remaining edges. A similar procedure has been supplemented in [12] and in the present paper by other derivation methods since our vector bases are always of additive kind, as opposite to what happen for the basis functions of [11], which simplify into the regular ones in case of singularity coefficient ν equal to unity.

In order to clarify the superior quality of our Table I bases with respect to that of other singular bases definable by *alternative methods*, this Appendix briefly reviews a method based on the use of special potentials to define singular divergence-less (solenoidal) basis functions on the singular elements, together with one singular edge-less function per element [18]. The edge-less function defined by these potentials is always related, by an appropriate dependency relation, to the edge-based solenoidal functions defined by the same potentials on the same element (see (26) and [18]).

At the lowest singular order, two solenoidal basis functions per singular element are obtained by defining two potentials $\phi_{i\pm1}$, each one associated with the element edge quoted in its subscript (see Fig. 1). Among the several possibilities to define appropriate potentials we consider, in particular, those summarized in Table IV. This Table reports four different potential families: the A1/A2-type and the B1/B2-type potentials, which all vanish at $\nu = 1$ in order to guarantee the additive kind of the singular vector functions they generate. ${}^{\square}\phi_{i\pm1}$ are the potentials of the edge-singularity quadrilateral, whereas ${}^{e}\phi_{i\pm1}$ and ${}^{v}\phi_{i\pm1}$ indicate the potentials for the edge- and the vertex-singularity triangles, respectively. These potentials vanish on all the element edges, with the exception of edge β quoted in their subscript. In terms of the dummy variable χ defined in (1), the expression of

TABLE IV
POTENTIALS TO BUILD SINGULAR DIVERGENCE-LESS FUNCTIONS

A1-Type	A2-Type
${}^{\square}\phi_{i\pm1}(\boldsymbol{r}) = \xi_{i\mp1}\left(\xi_i^{\nu}-\xi_i\right)$	${}^{\square}\phi_{i\pm1}(\boldsymbol{r}) = \xi_{i\mp1}\left(\nu\xi_i^{\nu}-\xi_i\right)$
${}^{e}\phi_{i\pm1}(\boldsymbol{r}) = \xi_{i\mp1}\frac{\left(\xi_i^{\nu}-\xi_i\right)}{1-\xi_i}$	${}^{e}\phi_{i\pm1}(\boldsymbol{r}) = \xi_{i\mp1}\frac{\left(\nu\xi_i^{\nu}-\xi_i\right)}{1-\xi_i}$
${}^{v}\phi_{i\pm1}(\boldsymbol{r}) = \xi_{i\mp1}\left[(1-\xi_i)^{\nu-1}-1\right]$	${}^{v}\phi_{i\pm1}(\boldsymbol{r}) = \xi_{i\mp1}\left[\nu\,(1-\xi_i)^{\nu-1}-1\right]$
$\phi_\beta(\chi) = \chi^{\nu}-\chi$	$\phi_\beta(\chi) = \nu\chi^{\nu}-\chi$
$\mathrm{d}\phi_\beta/\mathrm{d}\chi = \nu\chi^{\nu-1}-1$	$\mathrm{d}\phi_\beta/\mathrm{d}\chi = \nu^2\chi^{\nu-1}-1$

B1-Type	B2-Type
${}^{\square}\phi_{i\pm1}(\boldsymbol{r}) = \xi_{i\mp1}\xi_{i+2}\left(\xi_i^{\nu}-\xi_i\right)$	${}^{\square}\phi_{i\pm1}(\boldsymbol{r}) = \xi_{i\mp1}\xi_{i+2}\left(\nu\xi_i^{\nu}-\xi_i\right)$
${}^{e}\phi_{i\pm1}(\boldsymbol{r}) = \xi_{i\mp1}\left(\xi_i^{\nu}-\xi_i\right)$	${}^{e}\phi_{i\pm1}(\boldsymbol{r}) = \xi_{i\mp1}\left(\nu\xi_i^{\nu}-\xi_i\right)$
${}^{v}\phi_{i\pm1}(\boldsymbol{r}) = \xi_{i\mp1}\xi_i\left[(1-\xi_i)^{\nu-1}-1\right]$	${}^{v}\phi_{i\pm1}(\boldsymbol{r}) = \xi_{i\mp1}\xi_i\left[\nu\,(1-\xi_i)^{\nu-1}-1\right]$
$\phi_\beta(\chi) = (\chi^{\nu}-\chi)\,(1-\chi)$	$\phi_\beta(\chi) = (\nu\chi^{\nu}-\chi)\,(1-\chi)$
$\mathrm{d}\phi_\beta/\mathrm{d}\chi = \nu\chi^{\nu-1}-1$ $-\chi\left[(1+\nu)\,\chi^{\nu-1}-2\right]$	$\mathrm{d}\phi_\beta/\mathrm{d}\chi = \nu^2\chi^{\nu-1}-1$ $-\chi\left[\nu\,(1+\nu)\,\chi^{\nu-1}-2\right]$

the potential on the edge quoted in the subscript always simplifies into

$$ {}^{\square}\phi_\beta|_{\xi_\beta=0} = {}^{e}\phi_\beta|_{\xi_\beta=0} = {}^{v}\phi_\beta|_{\xi_\beta=0} = \phi_\beta(\chi) \tag{22} $$

with $\phi_\beta(\chi)$ explicitly reported in Table IV. The A1- and B1-type potentials, as well as the A2- and B2-type potentials, are equal in the limit for $\chi = 0$; in fact, for example, the ratio of $\phi_\beta(\chi)$ of the B-type potentials over the $\phi_\beta(\chi)$ of the A-type potentials is exactly equal to $(1-\chi)$.

By calling $\hat{n}$ the unit vector normal to the element face, the vector functions

$$ {}^{0}\boldsymbol{\Lambda}_{i\pm1} = \hat{\boldsymbol{n}} \times \boldsymbol{\nabla}\phi_{i\pm1} \tag{23} $$

generated by these potentials are divergence-less by construction and exactly tangent to the element edges where $\phi_{i\pm1}$ was set to zero. The potentials are constructed to guarantee that ${}^{0}\boldsymbol{\Lambda}_\beta$, in the direction normal to the βth edge, has a singular behavior in agreement with Meixner's theory. In fact, along side β, for $\beta = i \pm 1$, the normal components of the solenoidal functions is

$$ {}^{0}\boldsymbol{\Lambda}_\beta(\boldsymbol{r}) \cdot \hat{\boldsymbol{h}}_\beta|_{\xi_\beta=0} = \frac{1}{\ell_\beta}\frac{\mathrm{d}\phi_\beta}{\mathrm{d}\chi} \tag{24} $$

with $\mathrm{d}\phi_\beta/\mathrm{d}\chi$ also given in Table IV, and where $\hat{\boldsymbol{h}}_\beta(\xi_\beta = 0)$ is the unit outward normal to the element along its βth boundary edge, whereas ℓ_β is the magnitude of the edge-vector $\boldsymbol{\ell}_\beta$ along this same edge. Equation (24) guarantees the base-conformity, and in fact it is rather similar to (6).

Since the divergence of ${}^{0}\boldsymbol{\Lambda}_{i\pm1}$ is zero, a singular surface charge density has to be modelled by one edge-less function per element. Irrespective of whether one considers quadrilateral or triangular elements, and A- or B-type potentials, the required edge-less function $\mathbf{V}(\boldsymbol{r})$ and the relevant dependency relation can always be written as

$$ \mathbf{V}(\boldsymbol{r}) = \frac{\phi_{i-1}\boldsymbol{\ell}_{i-1} - \phi_{i+1}\boldsymbol{\ell}_{i+1}}{\mathcal{J}} \tag{25} $$

$$ \mathbf{V}(\boldsymbol{r}) + \xi_{i+1}^{0}\boldsymbol{\Lambda}_{i+1}(\boldsymbol{r}) - \xi_{i-1}^{0}\boldsymbol{\Lambda}_{i-1}(\boldsymbol{r}) = 0 \tag{26} $$

where, element by element, $\phi_{i\pm1}$ are the potentials belonging to one of the families of Table IV. Clearly, the polynomial coefficients that combine the vector functions in the dependency relation (26) have different order, as opposite to what happens for the dependency relations of Table I. This is a first drawback of divergence-conforming bases defined by potentials which renders the construction of higher order bases more difficult; in fact, it is not quite simple to use (26) to eliminate the dependency in the higher order vector sets obtained by applying the construction technique of Section IV. However, as we will see in the following, the major drawback of these lowest order bases with respect to those of Table I is that either some of their singular basis functions contain a fractional term, as it happens when using the A-type potentials ${}^{e}\phi_{i\pm1}$ on edge-singularity triangles, or that they contain some other spurious higher order term for the other elements (i.e., the quadrilateral and the triangular vertex-singularity element) in case one uses the B-type potentials. In MoM applications, the presence of these undesired terms considerably complicates the numerical evaluation of the required integrals to the desired accuracy [38].

In the following, for the sake of brevity, we discuss only the wedge-modelling properties of the vector functions obtained by using the A1-type potentials; although similar conclusions can be drawn for the bases provided by the other potentials of Table IV [18]. In particular, by using A1-potentials, one can prove that irrespective of whether one considers the edge singularity triangle or quadrilateral, the divergence-less current component parallel to the edge profile can be modelled by the following divergence-less linear combination of the lowest order edge-singularity basis functions

$$ \chi^{\nu-1}\frac{\boldsymbol{\ell}_i}{\mathcal{J}} = \frac{1}{\nu}\left\{\left[\boldsymbol{\Lambda}_{i+1}(\boldsymbol{r}) - \boldsymbol{\Lambda}_{i-1}(\boldsymbol{r})\right] - \left[{}^{0}\boldsymbol{\Lambda}_{i+1}(\boldsymbol{r}) + {}^{0}\boldsymbol{\Lambda}_{i-1}(\boldsymbol{r})\right]\right\} \tag{27} $$

which is a result similar to (7). For vertex singularity triangles, the A1-potentials also yield to the following result, similar to (13)

$$ \chi^{\nu-1}\frac{\boldsymbol{\ell}_i}{\mathcal{J}} = \frac{1}{\nu}\left\{\left[\boldsymbol{\Lambda}_{i+1}(\boldsymbol{r}) - \boldsymbol{\Lambda}_{i-1}(\boldsymbol{r})\right] + \left[{}^{0}\boldsymbol{\Lambda}_{i+1}(\boldsymbol{r}) + {}^{0}\boldsymbol{\Lambda}_{i-1}(\boldsymbol{r})\right]\right\} \tag{28} $$

Furthermore, still by using the A1-potentials, the vanishing normal component of the current density at the edge of the wedge is modelled by

$$ -\frac{\chi^{\nu}}{\ell_i} = \left[\boldsymbol{\Lambda}_{i+2}(\boldsymbol{r}) - \mathbf{V}(\boldsymbol{r})\right] \cdot \hat{\boldsymbol{h}}_i = \left[\boldsymbol{\Lambda}_{i+2}(\boldsymbol{r}) \pm^{0} \boldsymbol{\Lambda}_{i\pm1}(\boldsymbol{r})\right] \cdot \hat{\boldsymbol{h}}_i \tag{29} $$

for singularity quadrilaterals, whereas for edge-singularity triangles one has

$$ -\frac{\chi^{\nu}}{\ell_i} = -\left[\boldsymbol{\Lambda}_{i\pm1}(\boldsymbol{r}) + \mathbf{V}(\boldsymbol{r})\right] \cdot \hat{\boldsymbol{h}}_i. \tag{30} $$

Equations (29) and (30) prove that the modelling capability of the A1-bases is similar to that of (8) and (9), although one has to notice that, unfortunately, the normal component of the solenoidal functions of the edge-singularity triangle takes the rational expression

$$\pm{}^0\boldsymbol{\Lambda}_{i\pm1}(\boldsymbol{r})\cdot\hat{\boldsymbol{h}}_i = -\frac{\chi^\nu}{\ell_i} + \frac{\chi^\nu - 1}{\ell_i}\frac{\chi}{(\chi-1)} \tag{31}$$

which clearly contains a *dirty* term equal to ν/ℓ_i in the limit for $\chi = 1$ and that, for $\{0 \leq \chi < 1\}$, reads

$$\frac{\chi^\nu - 1}{\ell_i}\frac{\chi}{(\chi-1)} = \frac{(1-\chi^\nu)}{\ell_i}\sum_{n=1}^{+\infty}\chi^n. \tag{32}$$

This term complicates the numerical evaluation of the integrals required by MoM applications even though (32) vanishes at $\chi = 0$. To overcome this problem one can not simply resort to different potential functions. In fact, for example, by using B-type potentials one moves the undesired behavior involving higher order χ terms from the solenoidal functions of the edge-singularity triangle to the edgeless functions as well as to the solenoidal functions of the edge-singularity quadrilateral. Thus, the fact that the Meixner subset of Table I contains only two edge-singular triangular functions which satisfy (8) can now be further appreciated. To further clarify the superior modelling properties of our Table I bases, we point out that *all* the three A-type singular *vector* functions of the edge-singularity triangle do contain a rational term; in spite of the fact that the B-type functions and their divergence do not exhibit any rational term, the B-type *vector* functions do contain other higher order *dirty* terms in χ.

Finally, the singular charge density in the neighborhood of the wedge, that is for $\chi \simeq 0$, can be modelled by the divergence of the edgeless functions (25). In fact, for the A1-type quadrilateral basis functions, one has the following linear combinations:

$$\nu\frac{\chi^{\nu-1}}{\mathcal{J}} = \boldsymbol{\nabla}\cdot[\boldsymbol{\Lambda}_\beta(\boldsymbol{r}) - \mathbf{V}(\boldsymbol{r})] \tag{33}$$

where $\boldsymbol{\Lambda}_\beta(\boldsymbol{r})$, for $\beta = i$, $i \pm 1$, or $i+2$, is one of the regular quadrilateral functions. Similarly, (34) and (35) are the combinations that hold for the A1-type vertex-singularity and edge-singularity triangular functions, respectively, where $\boldsymbol{\Lambda}_\beta(\boldsymbol{r})$ now indicates one of the regular triangular functions obtained by choosing $\beta = i$, $i \pm 1$

$$\nu\frac{\chi^{\nu-1}}{\mathcal{J}} = \frac{\nu}{(1+\nu)}\boldsymbol{\nabla}\cdot[\boldsymbol{\Lambda}_\beta(\boldsymbol{r}) + \mathbf{V}(\boldsymbol{r})] \tag{34}$$

$$\nu\frac{\chi^{\nu-1}}{\mathcal{J}} + \frac{1}{\mathcal{J}}\frac{\chi^\nu - \chi}{\chi - 1} = \frac{1}{2}\boldsymbol{\nabla}\cdot[\boldsymbol{\Lambda}_\beta(\boldsymbol{r}) - 2\mathbf{V}(\boldsymbol{r})] \tag{35}$$

Once again, (35) contains an undesired term equal to $(\nu-1)/\mathcal{J}$ at $\chi = 1$, and that vanishes at $\chi = 0$; for $\{0 < \chi < 1\}$ this term reads

$$\frac{1}{\mathcal{J}}\frac{\chi^\nu - \chi}{\chi - 1} = \frac{(1-\chi^{\nu-1})}{\mathcal{J}}\sum_{n=1}^{+\infty}\chi^n \tag{36}$$

As said, B-type potentials simply move the undesired behavior involving higher order χ terms from (35) to (33) and (34).

REFERENCES

[1] A. W. Glisson and D. R. Wilton, "Simple and efficient numerical methods for problems of electromagnetic radiation and scattering from surfaces," *IEEE Trans. Antennas Propag.*, vol. 28, no. 5, pp. 593–603, Sep. 1980.

[2] J. R. Mautz, "Electromagnetic scattering from a thin rectangular plate" Jan. 1981, Electromagnetic Compatibility Analysis Center, Annapolis, MD, ESD-TR-81-100.

[3] S. M. Rao, D. R. Wilton, and A. W. Glisson, "Electromagnetic scattering by surfaces of arbitrary shape," *IEEE Trans. Antennas Propag.*, vol. 30, no. 3, pp. 409–418, May 1982.

[4] R. D. Graglia, D. R. Wilton, and A. F. Peterson, "Higher order interpolatory vector bases for computational electromagnetics," *IEEE Trans. Antennas Propag., Special Issue on Adv.Numer. Tech. Electromagn.*, vol. 45, no. 3, pp. 329–342, Mar. 1997.

[5] A. F. Peterson, S. L. Ray, and R. Mittra, *Computational Methods for Electromagnetics*, ser. IEEE/OUP Series on Electromagnetic Wave Theory. New York: IEEE Press, 1997.

[6] J. Meixner, "The behavior of electromagnetic fields at edges," *IEEE Trans. Antennas Propag.*, vol. AP-20, no. 4, pp. 442–446, Jul. 1972.

[7] J. Van Bladel, *Singular Electromagnetic Fields and Sources*. Oxford, U.K.: Clarendon, 1991.

[8] D. R. Wilton and S. Govind, "Incorporation of edge conditions in moment method solutions," *IEEE Trans. Antennas Propag.*, vol. 25, no. 6, pp. 845–850, Nov. 1977.

[9] J. Sercu, N. Fache, F. Libbrecht, and D. De Zutter, "Full-wave space-domain analysis of open microstrip discontinuities including the singular current-edge behavior," *IEEE Trans. Microw. Theory Tech.*, vol. 41, no. 9, pp. 1581–1588, Sep. 1993.

[10] T. Andersson, "Moment-method calculations on apertures using basis singular functions," *IEEE Trans. Antennas Propag.*, vol. 41, no. 12, pp. 1709–1716, Dec. 1993.

[11] W. J. Brown and D. R. Wilton, "Singular basis functions and curvilinear triangles in the solution of the electric field integral equation," *IEEE Trans. Antennas Propag.*, vol. 47, no. 2, pp. 347–353, Feb. 1999.

[12] R. D. Graglia and G. Lombardi, "Singular higher order complete vector bases for Finite Methods," *IEEE Trans. Antennas Propag.*, vol. 52, no. 7, pp. 1672–1685, Jul. 2004.

[13] *Fast and Efficient Algorithms in Computational Electromagnetics*, W. C. Chew, J.-M. Jin, E. Michielssen, and J. Song, Eds. Boston, MA: Artech House, 2001, ch. 6.

[14] H. Motz, "The treatment of singularities of partial differential equations by relaxation methods," *Quarterly Appl. Math.*, vol. 4, pp. 371–377, 1947.

[15] M. M. Bibby, A. F. Peterson, and C. M. Coldwell, "High-order basis functions for singular currents at corners," in *Proc. IEEE AP-S Int. Symp.*, Jun. 2007, pp. 5632–5635.

[16] R. D. Graglia, G. Lombardi, D. R. Wilton, and W. A. Johnson, "Modeling edge singularities in the method of moments," in *Proc. IEEE AP-S Int. Symp.*, Jul. 2005, vol. 3A, pp. 56–59.

[17] B. Khayatian, Y. Rahmat-Samii, and P. Y. Ufimtsev, "On the question of the imposition of the singular edge current behavior," in *Proc. IEEE AP-S Int. Symp.*, 2000, vol. 3, pp. 1558–1561.

[18] R. D. Graglia, "Scalar potentials and vector functions for the high-order modelling of singular wedge current," in *Antennas Propag. Int. Society Int. Symp.*, San Diego, CA, Jul. 5–11, 2008, pp. 1–4.

[19] J. C. Nedelec, "Mixed finite elements in R3," *Numer. Mathemat.*, vol. 35, pp. 315–341, 1980.

[20] K. R. Aberegg, A. Taguchi, and A. F. Peterson, "Application of higher-order vector basis functions to surface integral formulations," *Radio Sci.*, vol. 31, pp. 1207–1213, 1996.

[21] K. Hongo and H. Serizawa, "Diffraction of electromagnetic plane wave by a rectangular plate and a rectangular hole in the conducting plate," *IEEE Trans. Antennas Propag.*, vol. 47, no. 6, pp. 1029–1041, Jun. 1999.

[22] P. Savi, I.-L. Gheorma, and R. D. Graglia, "Full-wave high-order FEM model for lossy anisotropic waveguides," *IEEE Trans. Microw. Theory Tech.*, vol. 50, no. 2, pp. 495–500, Feb. 2002.

[23] R. D. Graglia and G. Lombardi, "Machine precision evaluation of singular and nearly singular potential integrals by use of Gauss quadrature formulas for rational functions," *IEEE Trans. Antennas Propag.*, vol. 56, no. 4, Apr. 2008.
[24] R. F. Harrington, *Field Computation by Moment Methods*. New York: Macmillan, 1968.
[25] R. F. Harrington, "Origin and development of the method of moments for field computation," in *Application of the Method of Moments to Electromagnetic Fields*, B. J. Strait, Ed. St. Cloud, FL: SCEEE Press, 1980, ch. 1.
[26] H. Moheb and L. Shafai, "Modal analysis method for bodies of arbitrary cross-section for numerical computation," *Inst. Elect. Eng. Proc.*, vol. 137, no. 5, pt. H, pp. 255–262, Oct. 1990.
[27] Y. Rahmat-Samii and R. Mittra, "Integral equation solution and RCS computation of a thin rectangular plate," *IEEE Trans. Antennas Propag.*, vol. 22, no. 4, pp. 608–610, Jul. 1974.
[28] Y. Rahmat-Samii and R. Mittra, "Correction to 'integral equation solution and RCS computation of a thin rectangular plate'," *IEEE Trans. Antennas Propag.*, vol. 23, no. 2, p. 302, Mar. 1975.
[29] *Electromagnetic and Acoustic Scattering by Simple Shapes*, J. J. Bowman, T. B. A. Senior, and P. L. E. Uslenghi, Eds. Amsterdam: North-Holland, 1969, ch. 14.
[30] T. B. A. Senior, "Disk scattering at edge-on incidence," *IEEE Trans. Antennas Propag.*, vol. 17, pp. 751–756, Nov. 1969.
[31] E. F. Knott, T. B. A. Senior, and P. L. E. Uslenghi, "High-frequency backscattering from a metallic disk," in *Proc. Inst. Elect. Eng.*, London, U.K., 1971, vol. 118, no. 12, pp. 1736–1742.
[32] S. W. Lee and P.L. E. Uslenghi, "High-frequency backscattering from an elliptic metal plate," *J. Math. Phys.*, vol. 15, pp. 631–639, 1974.
[33] D. P. Marsland, C. A. Balanis, and S. A. Brumley, "Higher order diffractions from a circular disk," *IEEE Trans. Antennas Propag.*, vol. 35, pp. 1436–1444, Dec. 1987.
[34] D.-W. Duan, Y. Rahmat-Samii, and J. P. Mahon, "Scattering from a circular disk: A comparative study of PTD and GTD techniques," *Proc. IEEE*, vol. 79, no. 10, pp. 1472–1480, 1991.
[35] H. Kobayashi and K. Hongo, "Scattering of electromagnetic plane waves by conducting plates," *Electromagn.*, vol. 17, pp. 573–587, 1997.
[36] C. J. Bouwkamp, "On the diffraction of electromagnetic waves by small circular disks and holes," *Philips Res. Rep.*, vol. 5, no. 6, pp. 401–422, Dec. 1950.
[37] R. W. Ziolkowski and W. A. Johnson, "Electromagnetic scattering of an arbitrary plane wave from a spherical shell with a circular aperture," *J. Math. Phys.*, vol. 28, no. 6, pp. 1293–1314, 1987.
[38] G. Lombardi, "Design of quadrature rules for Müntz and Müntzlogarithmic polynomials using monomial transformation," *Int. J. Numer. Methods Eng.*, submitted for publication.

Roberto D. Graglia (S'83–M'83–SM'90–F'98) was born in Turin, Italy, on July 6, 1955. He received the Laurea degree (*summa cum laude*) in electronic engineering from the Polytechnic of Turin in 1979, and the Ph.D. degree in electrical engineering and computer science from the University of Illinois at Chicago in 1983.

From 1980 to 1981, he was a Research Engineer at CSELT, Italy, where he conducted research on microstrip circuits. From 1981 to 1983, he was a Teaching and Research Assistant at the University of Illinois at Chicago. From 1985 to 1992, he was a Researcher with the Italian National Research Council (CNR), where he supervised international research projects. In 1991 and 1993, he was Associate Visiting Professor at the University of Illinois at Chicago. In 1992, he joined the Department of Electronics, Polytechnic of Turin, as an Associate Professor. He has been a Professor of Electrical Engineering at that Department since 1999. He has authored over 150 publications in international scientific journals and symposia proceedings. His areas of interest comprise numerical methods for high- and low-frequency electromagnetics, theoretical and computational aspects of scattering and interactions with complex media, waveguides, antennas, electromagnetic compatibility, and low-frequency phenomena. He has organized and offered several short courses in these areas.

Since 1997, he has been a Member of the editorial board of ELECTROMAGNETICS. He is a past associate editor of the IEEE TRANSACTIONS ON ANTENNAS AND PROPAGATION and a past associate editor of the IEEE TRANSACTIONS ON ELECTROMAGNETIC COMPATIBILITY. He is currently an associate editor of the IEEE ANTENNAS AND WIRELESS PROPAGATION LETTERS, and a Reviewer for several international journals. He was the Guest Editor of a special issue on Advanced Numerical Techniques in Electromagnetics for the IEEE TRANSACTIONS ON ANTENNAS AND PROPAGATION in March 1997. He has been Invited Convener at URSI General Assemblies for special sessions on Field and Waves in 1996, Electromagnetic Metrology in 1999, and Computational Electromagnetics in 1999. He served the International Union of Radio Science (URSI) for the triennial International Symposia on Electromagnetic Theory as Organizer of the Special Session on Electromagnetic Compatibility in 1998 and was the co-organizer of the special session on Numerical Methods in 2004. Dr. Graglia served the IEEE Antennas and Propagation Society as a member of its Administrative Committee (AdCom), for the triennium 2006–2008. Since 1999, he has been the General Chairperson of the biennial International Conference on Electromagnetics in Advanced Applications (ICEAA), held in Turin.

Guido Lombardi (S'02–M03) was born in Florence, Italy, on December 8, 1974. He received the Laurea degree (*summa cum laude*) in telecommunications engineering from the University of Florence, Florence, Italy, in 1999, and the Ph.D. degree in electronics engineering from the Polytechnic of Turin, Turin, Italy, in January 2004. His Ph.D. work focused on the study of analytical and numerical aspects of electromagnetic singularities.

From 2000 to 2001, he was an Officer of the Italian Air Force. In 2004, he joined the Department of Electronics, Polytechnic of Turin, as an Associate Researcher. He has been an Assistant Professor at that Department since 2005. His research areas comprise numerical methods for electromagnetics, theoretical and computational aspects of FEM and MoM, Wiener-Hopf method, electromagnetic singularities, waveguide problems, microwave passive components and project of orthomode transducers (OMT).

Dr. Lombardi received the Raj Mittra Travel Grant Award, as a junior researcher, at the 2003 IEEE AP-S International Symposium and USNC/CNC/URSI National Radio Science Meeting, Columbus, OH. In the same year he spent two months as Research Visitor at the Department of Electrical and Computer Engineering, University of Houston, Houston, TX. Since 2001, he served as a member of the Organizing Committee of the biennial International Conference on Electromagnetics in Advanced Applications (ICEAA), held in Turin. He is currently a Reviewer for several international journals.